SUPPORTING INFORMATION

Optimal selection of RuO_2 for durable oxygen evolution reactions in acid by continuous regulating of Ru-O covalency

Xintong Li,[§a] Guanzhen Chen,[§a] Yan Liu, [§b] Ruihu Lu,[b] Chao Ma,[c] Ziyun Wang, *[b] Yunhu Han*[a] and Dingsheng Wang[c]

Table of Contents

Section S1. Experimental Procedure

1.1 Synthesis Procedures

Materials. The chemicals and reagents were used as received. Sodium chloride (NaCl 99%), lithium chloride (LiCl 99%), chromium acetylacetonate ($C_{15}H_{21}CrO_6$, 97%), ruthenium acetylacetonate ($C_{15}H_{21}O_6Ru$, 99%), were purchased from Shanghai Titan Technology Co., Ltd. The commercial Pt/C catalyst is 20 wt.% by wt. of ~3 nm platinum nanoparticles on XC-72 carbon and nafion D-521 dispersion (5% w/w in water and 1-propanol) were obtained from Alfa Aesar. Doubly distilled deionized water (18.2 MΩ) was used for all experiments.

Experimental Section.

Preparation of $Cr_xRu_{1-x}O_2$. Typically, Sodium chloride and lithium chloride with a weight of 80 mg and 120 mg and ruthenium acetylacetonate and chromium acetylacetonate were ground evenly in a mortar according to the calculated ratio, and the obtained powder was transferred into a porcelain boat and put into a muffle furnace to anneal in an air atmosphere at 400 ℃ for 2 h. Immediately after the end of the annealing, the powder was cooled down with different media and leached in acid with 0.1 M HCl for 12 h. After the end of the etching, the powder was centrifuged, and washed with deionized water for three times. Finally, the obtained sample was dried in an oven at 80℃ for 12h to obtain $Cr_xRu_{1-x}O_2$ catalyst. RuO_2, $Cr_{0.16}Ru_{0.84}O_2$, $Cr_{0.22}Ru_{0.78}O_2$, $Cr_{0.31}Ru_{0.69}O_2$, $Cr_{0.48}Ru_{0.52}O_2$, $Cr_{0.64}Ru_{0.36}O_2$ and $Cr_{0.71}Ru_{0.29}O_2$ catalysts were prepared using the same procedure, and all cooled with water.

PEMWE test. For electrolysis tests, a self-made cell was used as the PEMWE device and a cation exchange membrane (Nafion 117) as the membrane electrolyte. In our initial trial, around 0.5 mg cm^{-2} commercial Pt/C with 20 wt.%, ~2 mg cm^{-2} OER catalyst with 20 wt.% polytetrafluoroethylene binder was sprayed onto sheets of polytetrafluoroethylene (PTFE) (surface area 2 × 2 cm^2) a platinized titanium felt electrode. After drying, the electrode was pressed at 100 °C for 5 min under a low pressure of 5 MPa by a regular hotpress machine. The PEMWE device was constructed by PTFE-supported Pt/C cathode catalyst, pretreated N117 membrane and PTFE-supported $Cr_xRu_{1-x}O_2$ anode catalysts, which was then circulated with deionized water at 400 ml min^{-1}. I–V curves were measured in galvano-static mode at 50–2000 mA cm^{-2} at room temperature and ambient pressure. The stability test was carried out at 1 A cm^{-2} at 80 °C and ambient pressure.

Estimation of hydrogen produced and cost in PEMWE.

The calculation of hydrogen cost in PEMWE was based on the reported work. Specifically,

$$Mass\ of\ H_2 = \frac{j(current\ density) \times A(electrolyzer\ area) \times t(working\ time) \times Molar\ mass\ H_2}{2 \times F} = 103g \quad (1)$$

$$Cost\ per\ kilogram\ of\ H_2 = energy\ consumption \times electricity\ bill = \frac{1.53 \times 1.2\ A \times 2300\ h}{0.103\ kg\ H_2} \times \frac{USD\ 0.02}{kWh} = \frac{USD\ 0.82}{kg\ H_2}$$

1.2 Material characterizations

Characterizations. The microstructure and morphology of the prepared materials was observed by a transmission electron microscope (TEM; HT7800) and high-resolution transmission electron microscopy (HRTEM; FEI-Themis Z TEM/STEM operated at 300 kV and equipped with double spherical aberration (Cs) correctors, Themis Z TEM/STEM equipped with high angle annular dark field (HAADF) and annular bright field (ABF) detectors). The HAADF images were acquired using the Themis Z with a 59~100 mrad inner-detector angle. The attainable resolution of the probe defined by the objective pre-field is 60 picometers. A Super X Windowless X-ray detector was used to collect the energy dispersive spectra (EDS). XPS was performed on a KULVAC PHI Quantera X-ray photoelectron spectrometer and analyzed by the Avantage software. X-ray powder diffraction (XRD) patterns were obtained by a Bruker D8 Advances using Cu Kαradiation (λ= 1.5406 Å). The X-ray absorption fine structure spectra (Ru K-edge, Cr K-edge) were collected at 1W1B station in Beijing Synchrotron Radiation Facility (BSRF). The storage rings of BSRF were operated at 2.5 GeV with an average current of 250 mA. Using Si (111) double-crystal monochromator, the data collections were carried out in S4 transmission/fluorescence mode using ionization chamber. All spectra were collected in ambient conditions.

In-situ ATR-FTIR measurement. The in-situ ATR-IR monitoring process was carried out using a Nicolet 6700 FTIR spectrometer armed with an MCT detector and a PIKE VeeMAX III ATR accessory. A single cell with 25 ml of 0.5 M H_2SO_4 electrolyte was used as the reactor. The working electrode was glass carbon. Ag/AgCl was used as the reference electrode, while a Pt wire was used as the counter electrode. Before starting the tests, the device was purged with ultrapure water and the electrolyte was treated for 30 min. Then, N_2 was introduced into the electrolyte for 30 min to achieve N_2 saturation. The background spectrum was collected with no potential applied, and spectra were recorded during the electrolysis procedure under different potentials. A 4 cm^{-1} resolution and 32 scans were applied in the collection of all the spectra. Potentials were corrected with respect to a reversible hydrogen electrode.

DEMS tests. For in situ differential electrochemical mass spectrometry measurements (DEMS), we measured the LSV curves in a three-electrode cell by using the ^{18}O isotope-labeling $Cr_{0.31}Ru_{0.69}O_2$-coated electrodes in N_2-saturated 0.5 M H_2SO_4 with $H_2{}^{16}O$ for catalyzing the

OER. (i) 0.5 M H_2SO_4 solution with $H_2{}^{18}O$ was used as solvent to obtain the ^{18}O isotope-labeling $Cr_{0.31}Ru_{0.69}O_2$ electrodes. (ii) $H_2{}^{16}O$ was used to remove the residual $H_2{}^{18}O$ on the surface for the above ^{18}O isotope-labeling $Cr_{0.31}Ru_{0.69}O_2$ electrodes. (iii) The respective LSV cycles were measured for ^{18}O isotope-labeling $Cr_{0.31}Ru_{0.69}O_2$ electrodes in 0.5 M H_2SO_4 solution using $H_2{}^{16}O$ as electrolyte in the potential range of 0.8-1.6 V vs. RHE with a scan rate of 0.5mV s^{-1}, which then the gaseous products of $^{36}O_2$, $^{34}O_2$ and $^{32}O_2$ were monitored by the mass spectrometer. The ratio of $^{36}O_2$, $^{34}O_2$, and $^{32}O_2$ can be estimated by calculating the integral areas for the corresponding mass signals.

1.3 Electrochemical measurements

Electrochemical Measurements. Electrochemical measurements were conducted on a CHI 760E Electrochemical Workstation (Shanghai Chenhua Instrument Corporation, China) in a conventional three-electrode cell. The graphite rod electrode as the counter electrode, and an Ag/AgCl (saturated KCl solution) as the reference electrode, the working electrode was a glassy carbon electrode (GCE, diameter: 5 mm, area: 0.1963 cm^2). Conversion from the SCE reference electrode to RHE was done according to E (vs. RHE) = E (vs. Ag/AgCl) + 0.0591×pH+0.197. The working electrode was prepared as follows: 2.5 mg of catalyst was dispersed in the mixture of ethanol (0.4 mL) and Nafion (5 wt%, 30 μL) under ultrasonication for 1 h, catalyst with the concentration of 7.5 mg mL^{-1} was obtained. 10 μL of the catalyst was dropped onto the GCE surface for further electrochemical tests. All the potentials reported in this work were converted to the reversible hydrogen electrode (RHE). All measured potentials in RDE tests were 95% iR compensated unless otherwise specified. LSV tests were recorded at a scan rate of 5 mV s^{-1}. Stability was examined by chronopotentiometry testing at 10 mA cm^{-2} in 0.5 M H_2SO_4. Cyclic voltammograms (CVs) were performed in N_2-saturated 0.5 M H_2SO_4 solution from 1.15 to 1.35 V (RHE) at a scan rate of 50 mV·s^{-1}. Electrochemical impedance spectroscopy (EIS) measurements were measured at 50 mV vs. RHE in the frequency range from 10 kHz to 0.01 Hz in N_2-saturated 0.5 M H_2SO_4 solution. The electrochemical active surface area was estimated from the electrochemical double layer capacitance (C_{dl}) from equation (3).

$$ECSA = \frac{Cdl}{Cs} \quad (3)$$

The value for C_{dl} was determined via CV scanning in a non-Faradic region from 1.12 to 1.22 V vs. RHE with scanning rate, 2.5, 5.0, 7.5, 10, 15, and 20 mV s^{-1}. The value of the slope was determined from fitting of the data to obtain C_{dl}. The specific current density per ECSA was computed via normalizing the current by ECSA, a general specific capacitance of C_s = 0.035 mF cm^{-2} was used based on typicalreported values. The roughness factor (R_f) was calculated by dividing ECSA by the geometric area of the electrode of 0.196 cm^{-2} in this work. The amount of Ru dissolved was measured by ICP-MS.

Density function theory calculations. All calculations in the paper were carried out with the Perdew–Burke–Ernzerhof (PBE) functional using Vienna ab initio simulation package (VASP)[1, 2]. The project-augmented wave (PAW) method was used to represent the core–valence interaction[3, 4]. For the calculations of total energy, a cut-off energy of 500 eV was set for plane wave basis sets to expand the valence electronic states. Spin polarization was included for all calculations to obtain an accurate description of magnetic systems. The D3BJ correction method[5] was employed in order to include van der Waals (vdW) interactions. For optimization, kpoint sampling with a (2 × 2 × 1) mesh within the Monkhorst−Pack scheme was utilized, as the length of the slab cell is 9.37 Å× 12.80 Å× 23.86 Å. A vacuum layer of 15 Å was applied to avoid lateral interactions, and the geometry optimization and energy calculations were finished when the electronic self-consistent iteration and force reached 10^{-5} eV and 0.05 eV/Å respectively. All models are shown in Figure S29.

OER. The OER could occur in the following four elementary steps:

$$OH^- + * \rightarrow *OH + e^- \quad (4)$$

$$*OH + OH^- \rightarrow *O + H_2O + e^- \quad (5)$$

$$*O + OH^- \rightarrow *OOH + H_2O + e^- \quad (6)$$

$$*OOH + OH^- \rightarrow * + O_2 + H_2O + e^- \quad (7)$$

where * denotes the active sites on the catalyst surface.

The Gibbs Free Energy Change. The change in the Gibbs free energy (ΔG) of each elemental steps were adsorbed intermediate was calculated based on the computational hydrogen electrode (CHE) method developed by Nørskov et al[6]. Under standard conditions (T = 298.15 K, pH = 0, and U = 0 V (vs. SHE)), the ΔG is defined by the following equation. Based on this, the free energy of OER is calculated as follows:

$$\Delta G_{ads} = \Delta E_{ads} + \Delta E_{ZPE} - T\Delta S_{ads} \quad (8)$$

where ΔE_{ads} is the electronic adsorption energy, ΔE_{ZPE} is the zero point energy difference between adsorbed and gaseous species, T is the temperature (298.15 K) in then above reaction system, and ΔS represents the difference on the entropies between the adsorbed state and gas phase. Charge density and differences are calculated using Bader code[7]. For energy correction of the result, use the energy of OH is H_2O-1/2 H_2. The source of entropy is the NIST Chemistry Webbook (https://webbook.nist.gov/chemistry/). The electronic binding energy is referenced as ½ H_2 for each H atom, and (H_2O-H_2) for each O atom, plus the energy of the clean slab. The corrections of zero-point energy and entropy of the OER intermediates can be found in Table S7.

Supplementary Figures

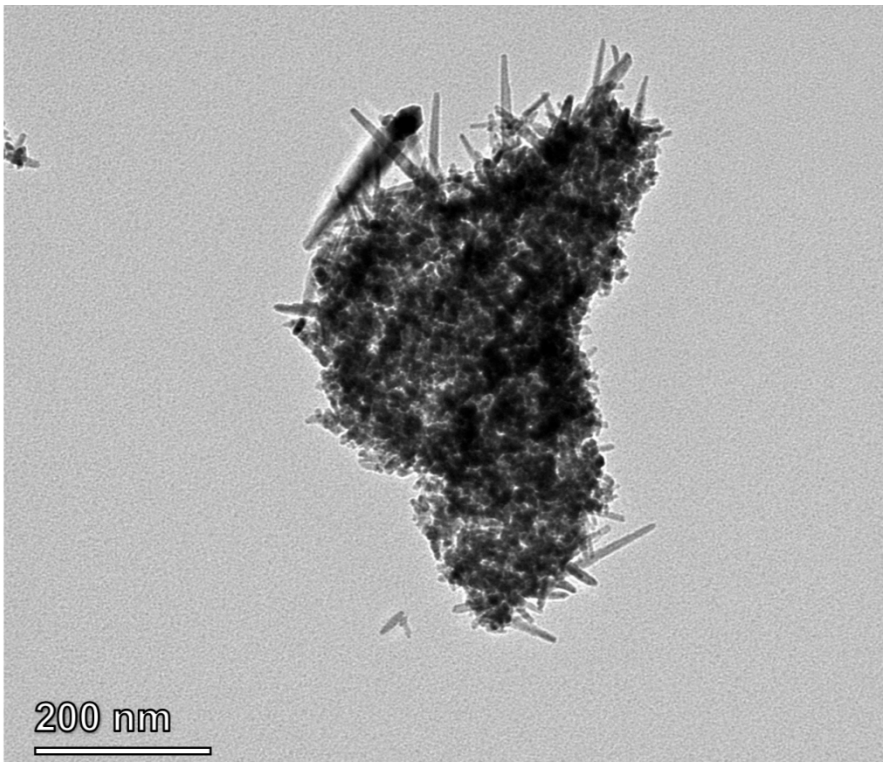

Fig. S1 The TEM images of homemade RuO_2.

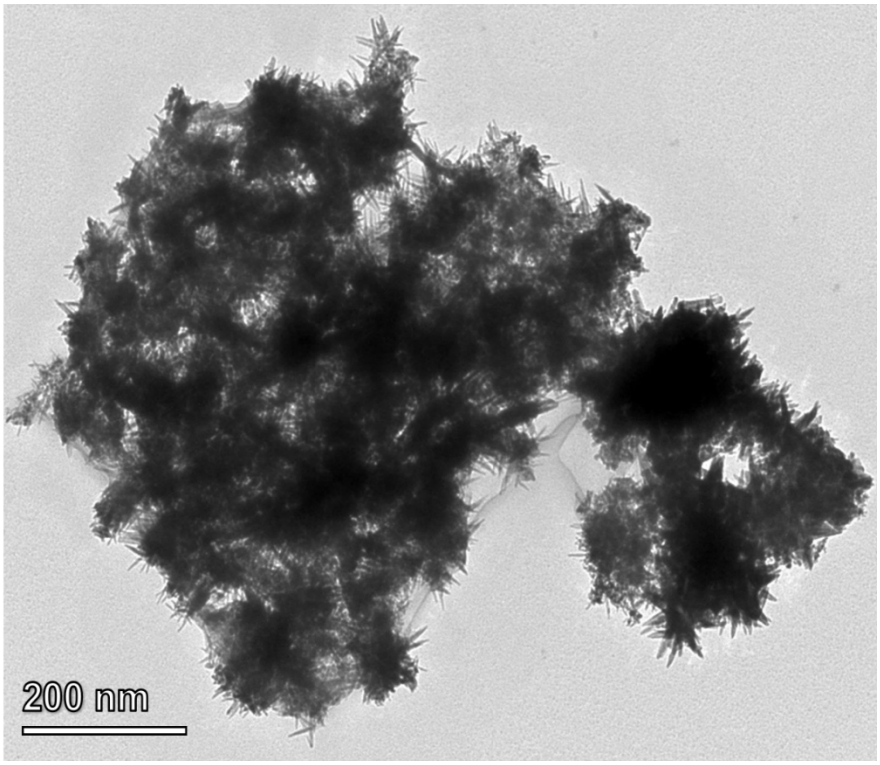

Fig. S2 The TEM images of $Cr_{0.16}Ru_{0.84}O_2$.

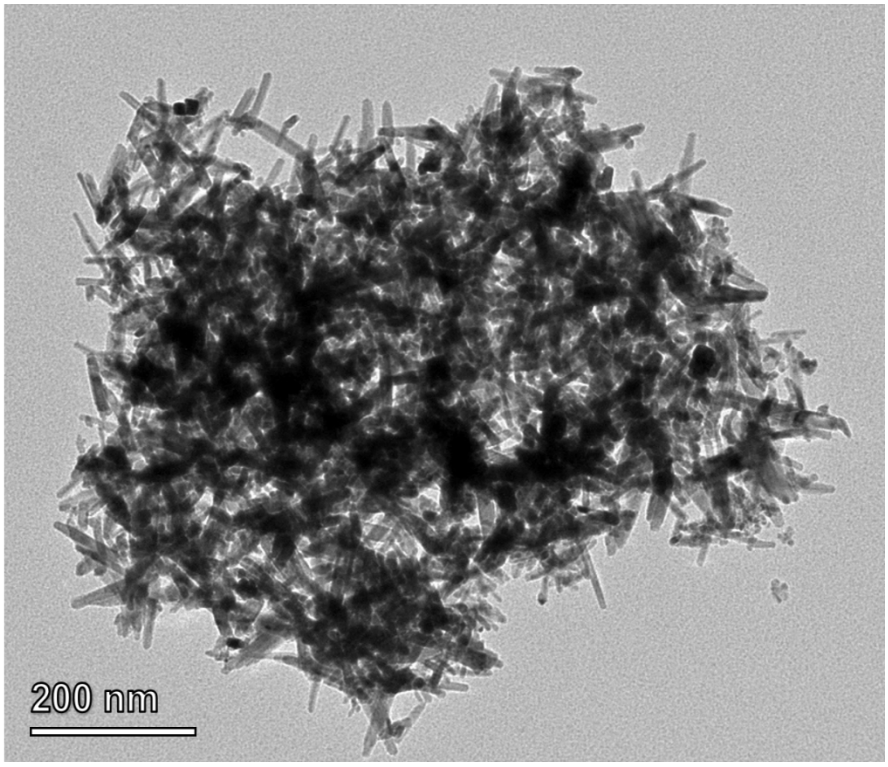

Fig. S3 The TEM images of $Cr_{0.22}Ru_{0.78}O_{2.}$

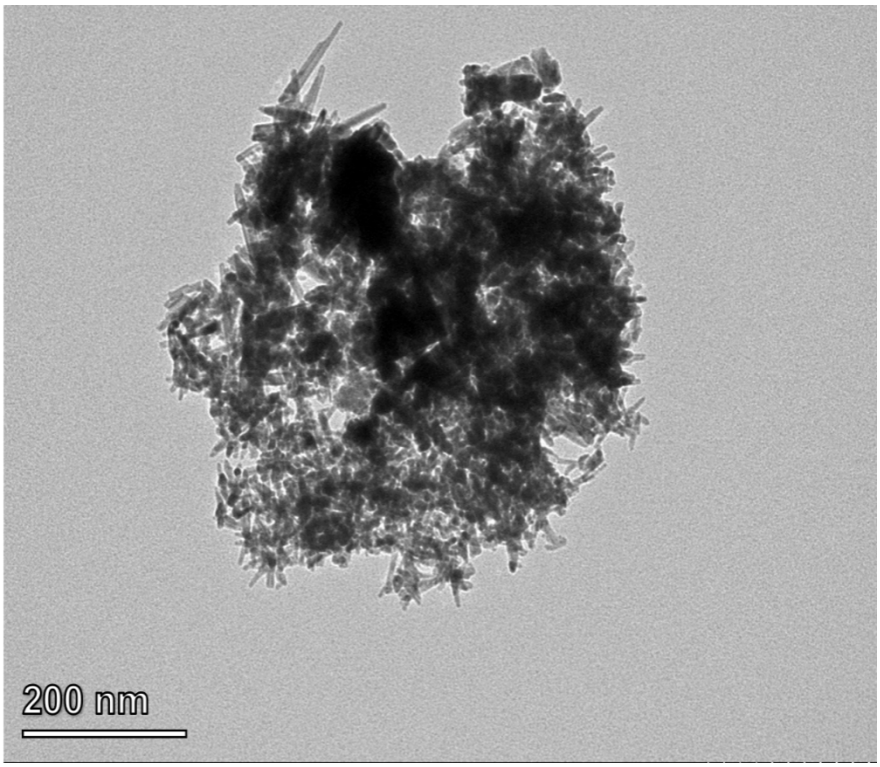

Fig. S4 The TEM images of $Cr_{0.48}Ru_{0.52}O_2$.

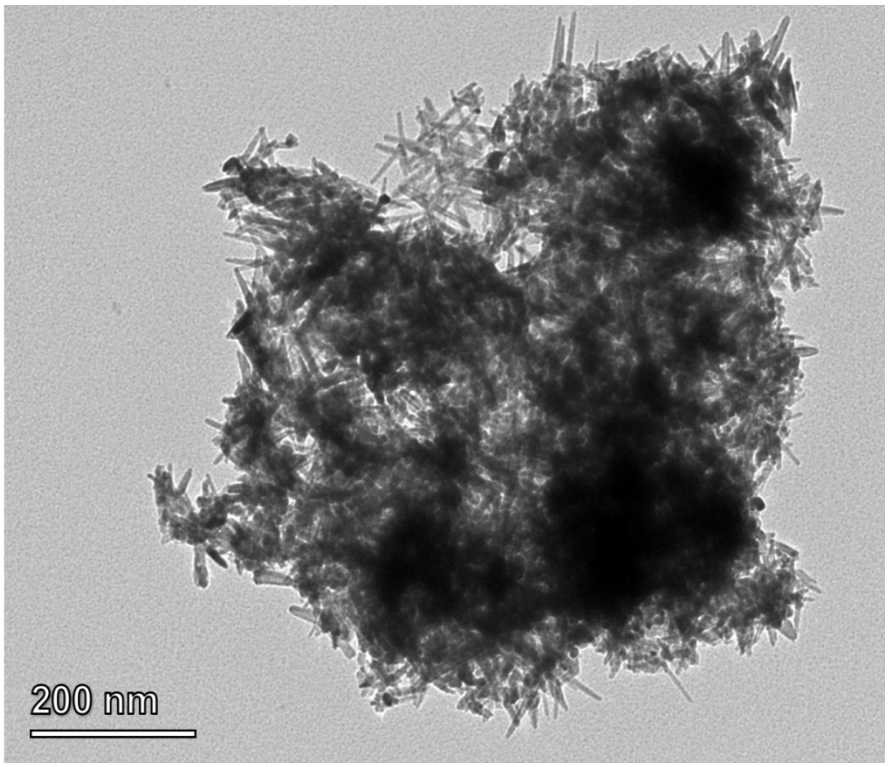

Fig. S5 The TEM images of $Cr_{0.64}Ru_{0.36}O_2$.

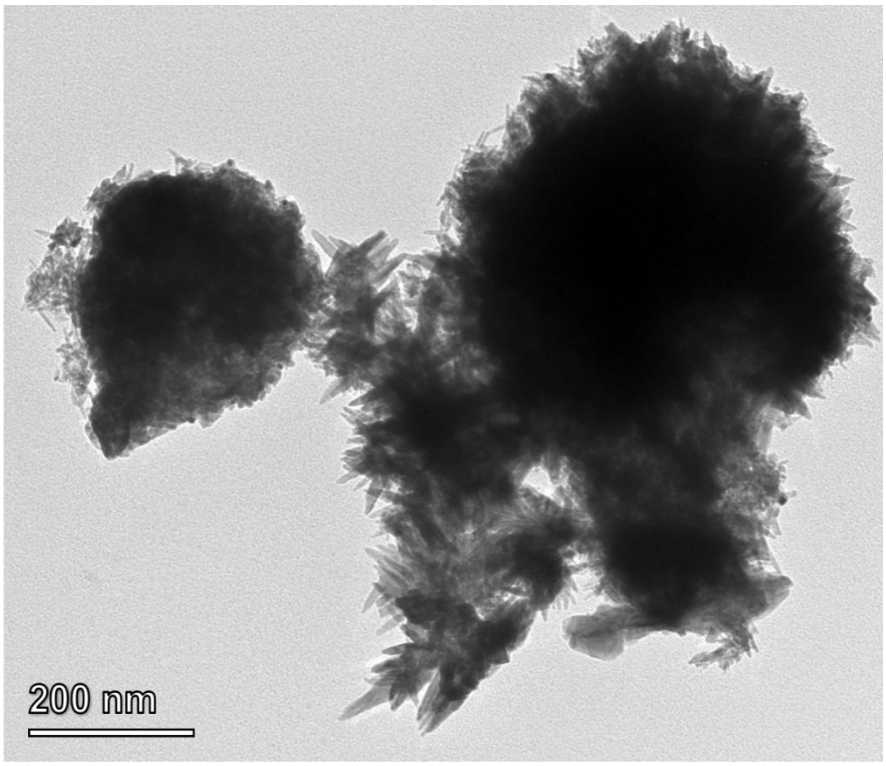

Fig. S6 The TEM images of $Cr_{0.71}Ru_{0.29}O_2$.

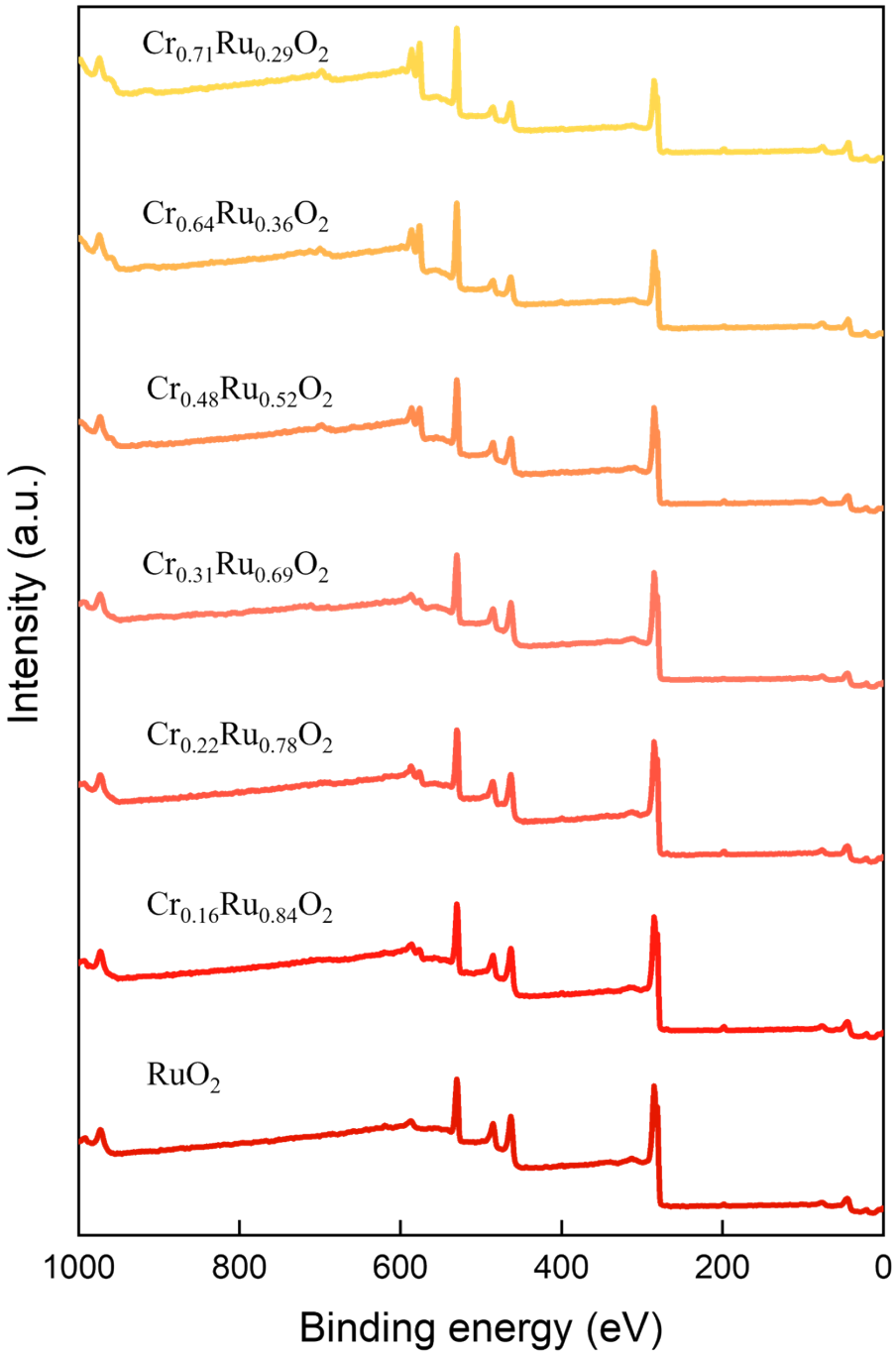

Fig. S7 The XPS survey spectra of $Cr_xRu_{1-x}O_2$.

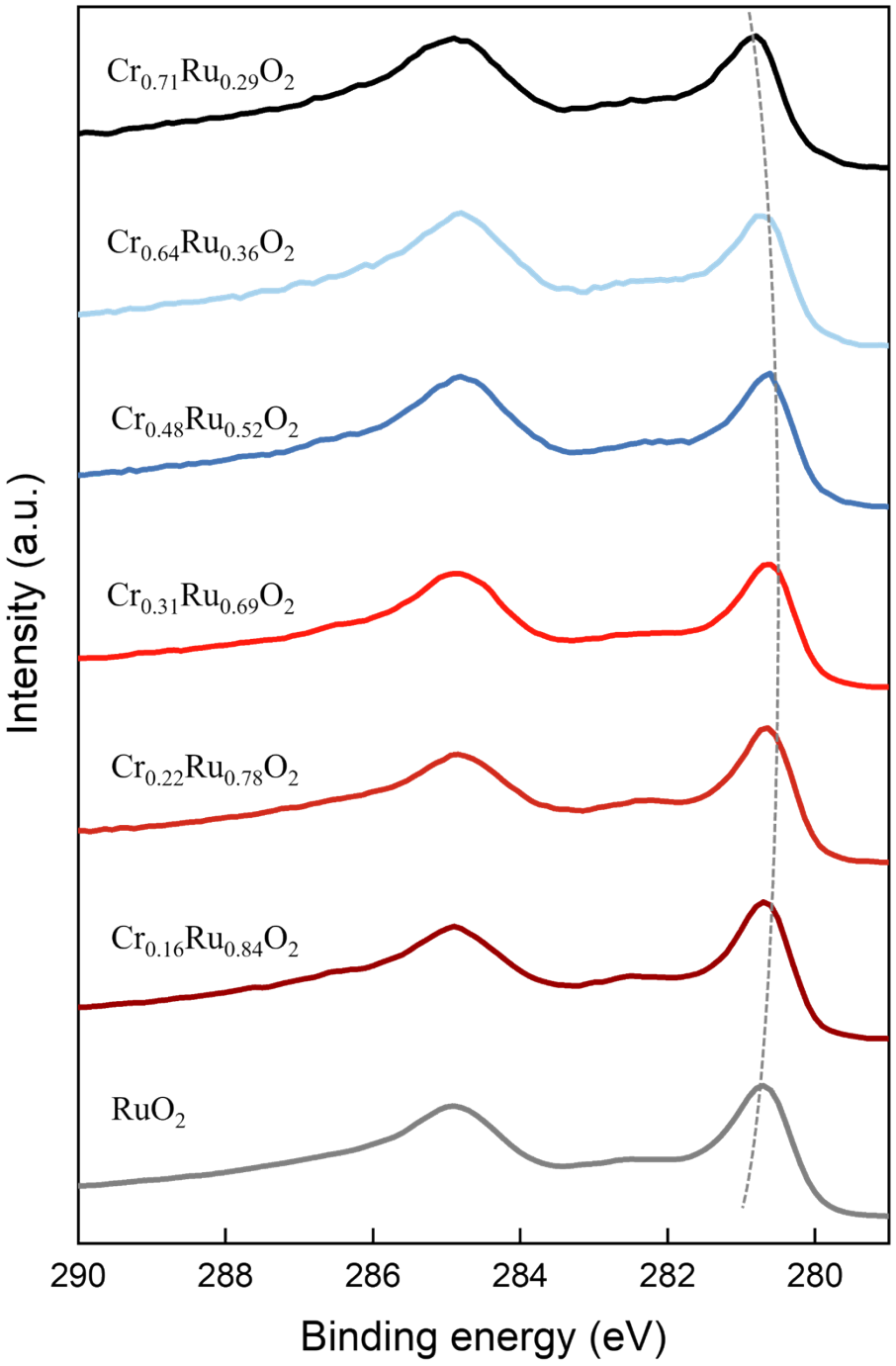

Fig. S8 Ru 3d spectra of $Cr_xRu_{1-x}O_2$.

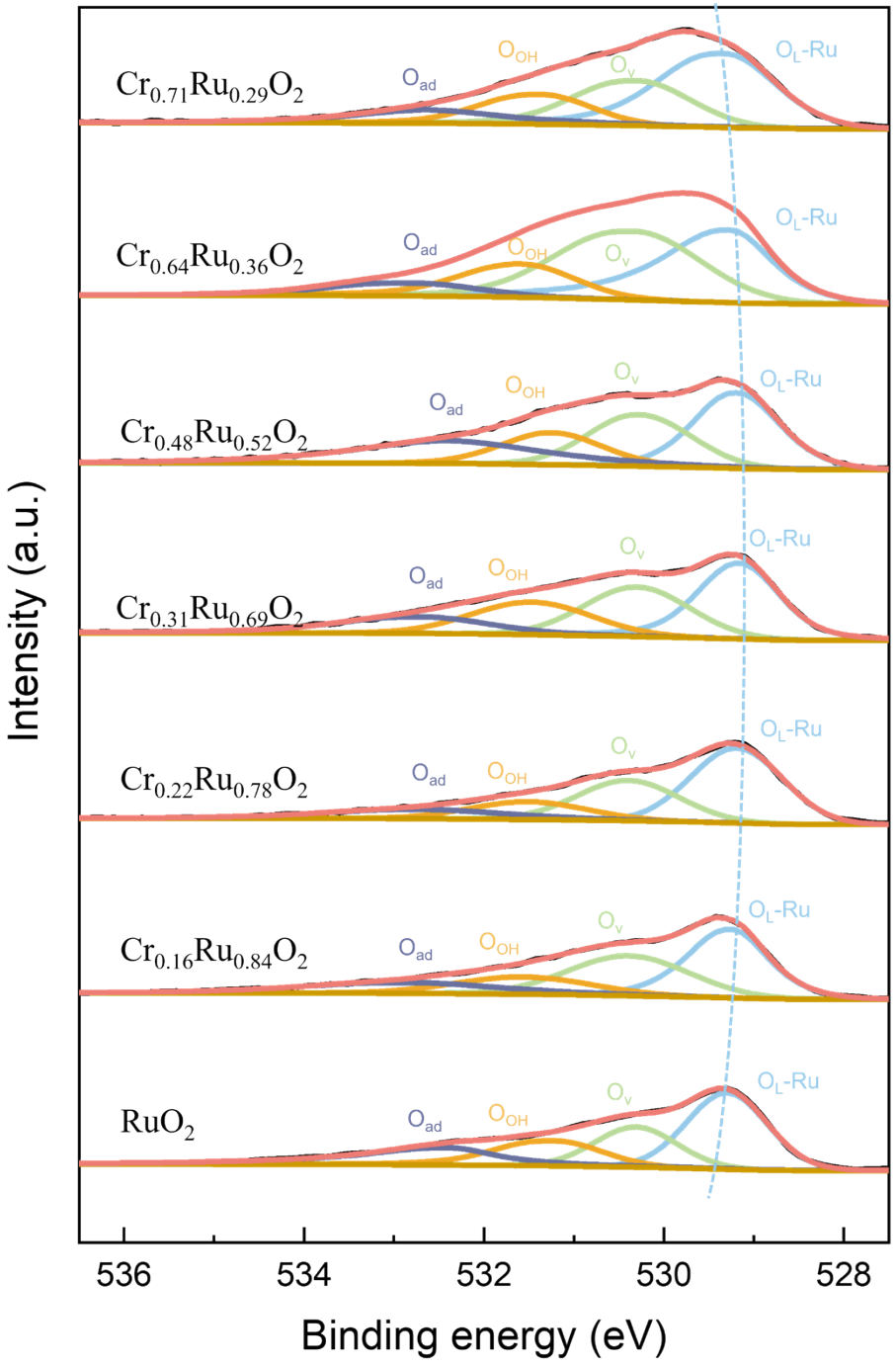

Fig. S9 1s spectra of $Cr_xRu_{1-x}O_2$.

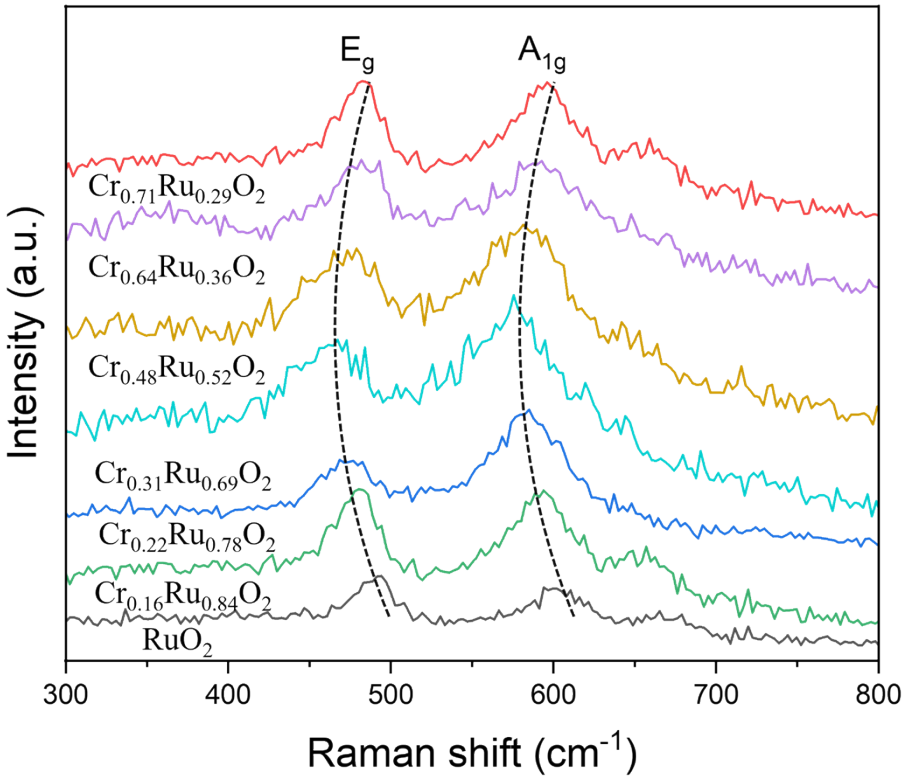

Fig. S10 Raman spectra of $Cr_xRu_{1-x}O_2$.

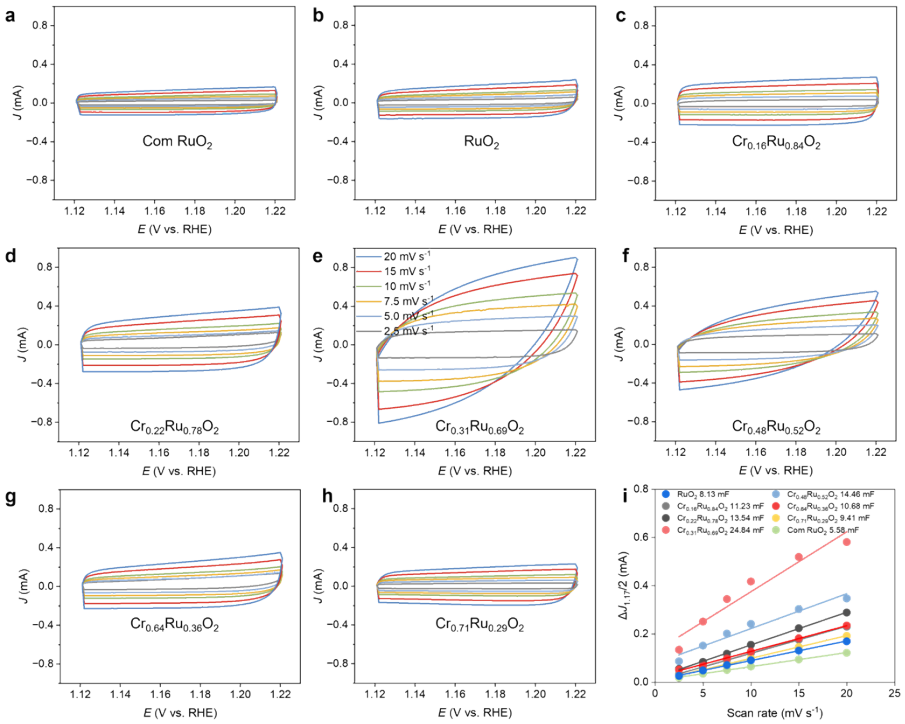

Fig. S11 (a-h) CVs for $Cr_xRu_{1-x}O_2$, Com RuO_2 and RuO_2 catalysts at different scan rates from 2.5 to 20 mV s^{-1}, respectively. (i) C_{dl} plots derived from CV curves.

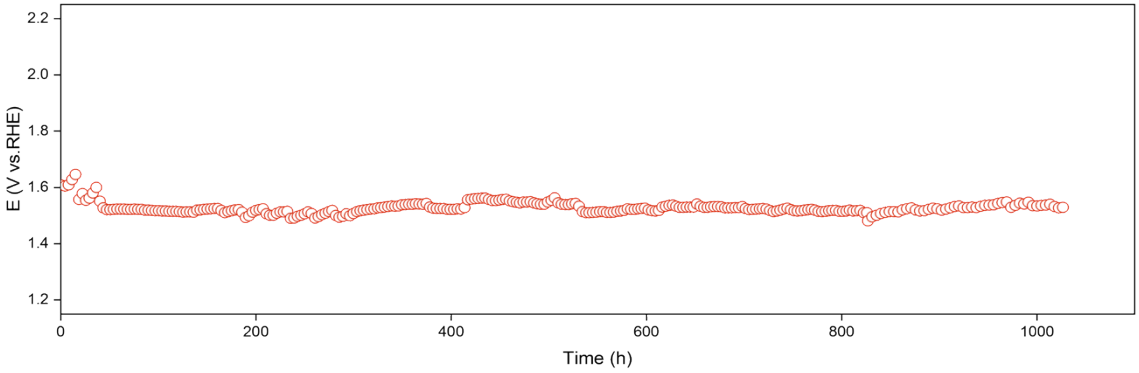

Fig. S12 The OER durability of $Cr_{0.31}Ru_{0.69}O_2$ under density of 250 mA cm^{-2}.

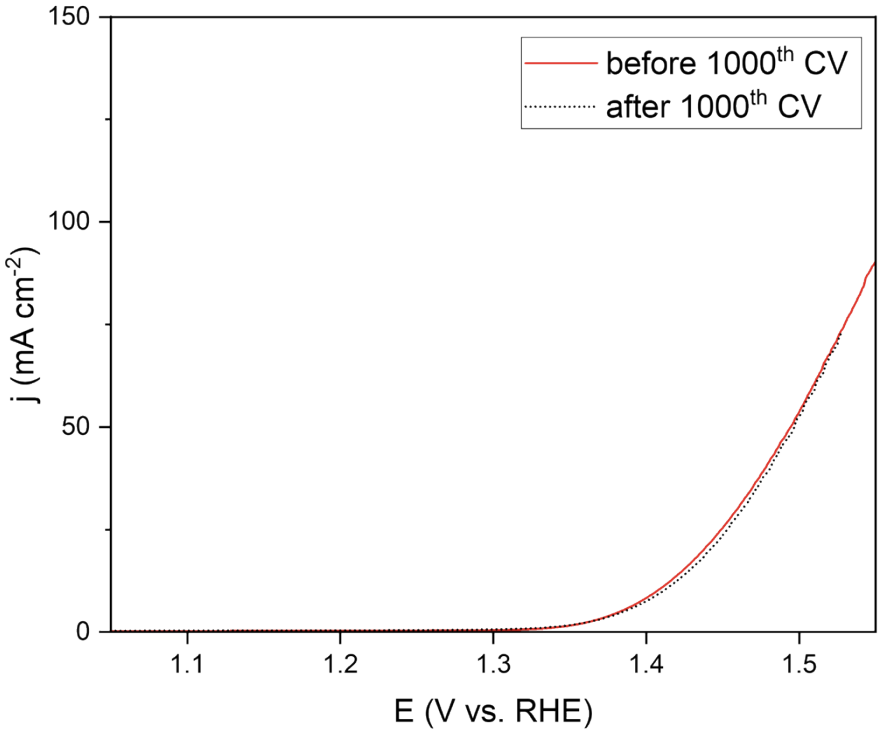

Fig. S13 LSV curves of before and after 1000th cycles for $Cr_{0.31}Ru_{0.69}O_2$.

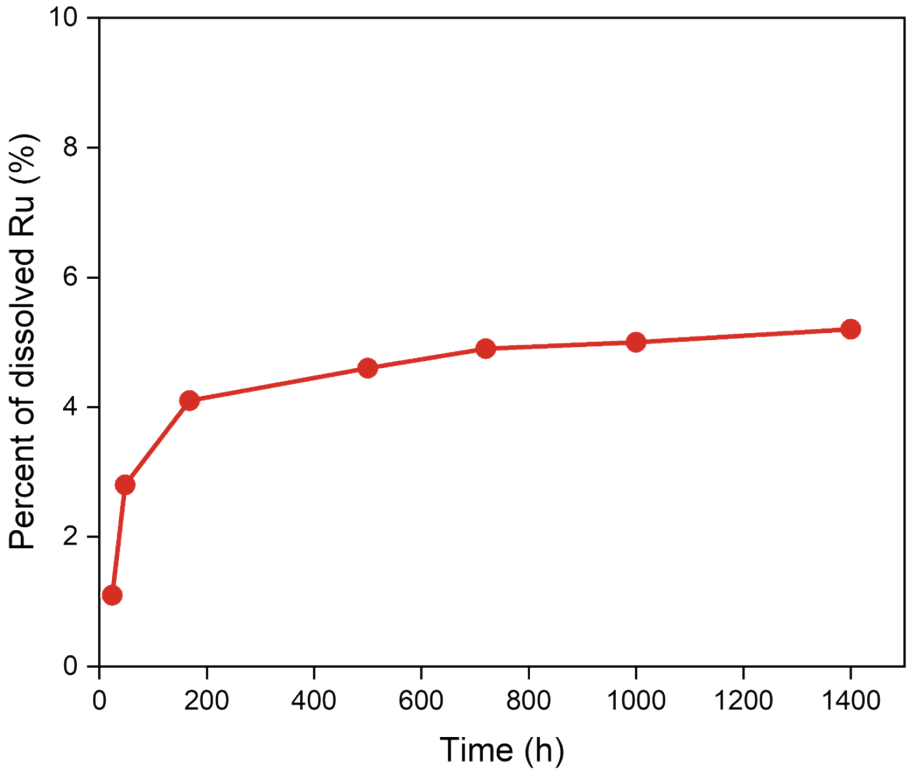

Fig. S14 Time-dependent ion dissolution of $Cr_{0.31}Ru_{0.69}O_2$ during OER.

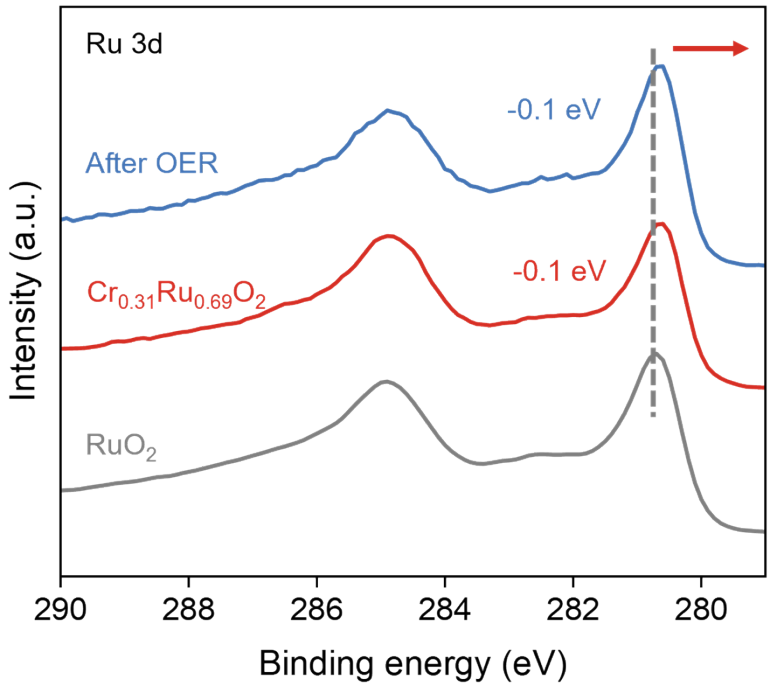

Fig. S15 Ru 3d spectra of $Cr_{0.31}Ru_{0.69}O_2$ before and after 48 h catalysis stability test.

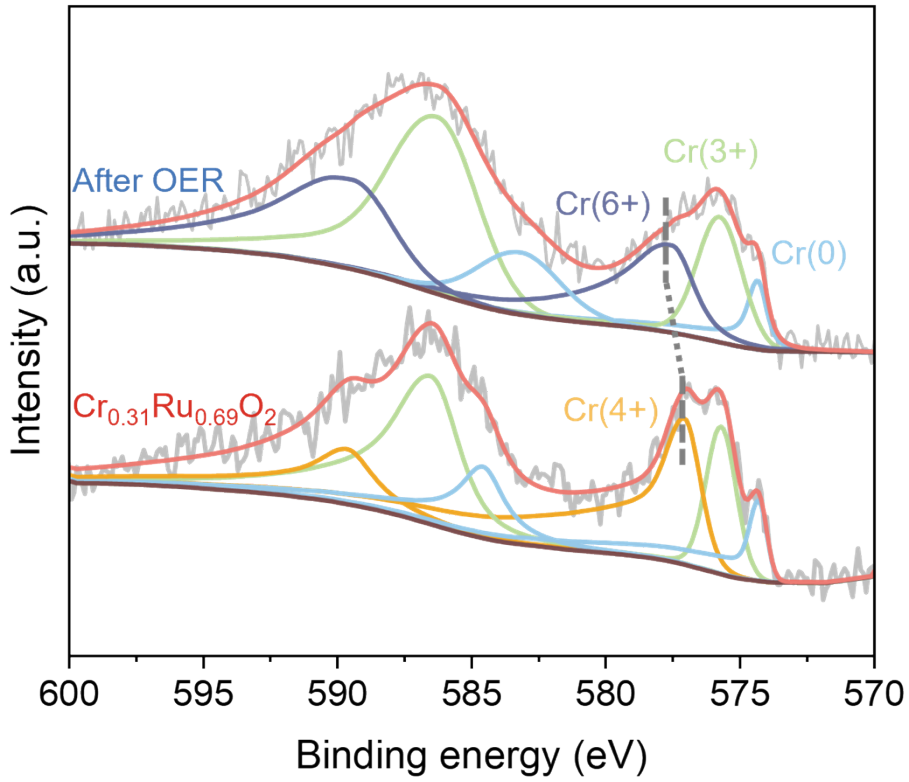

Fig. S16 Cr 2p spectra of $Cr_{0.31}Ru_{0.69}O_2$ before and after 48 h catalysis stability test.

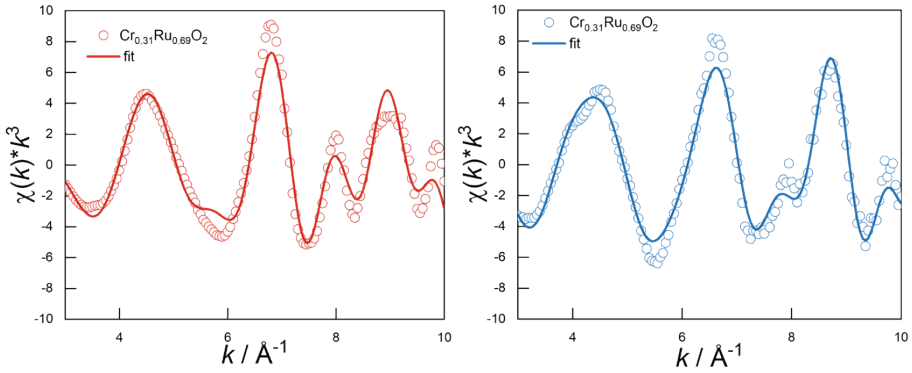

Fig. S17 k^3-weighted k space fitting curves of $Cr_{0.31}Ru_{0.69}O_2$ and corresponding fitting curve.

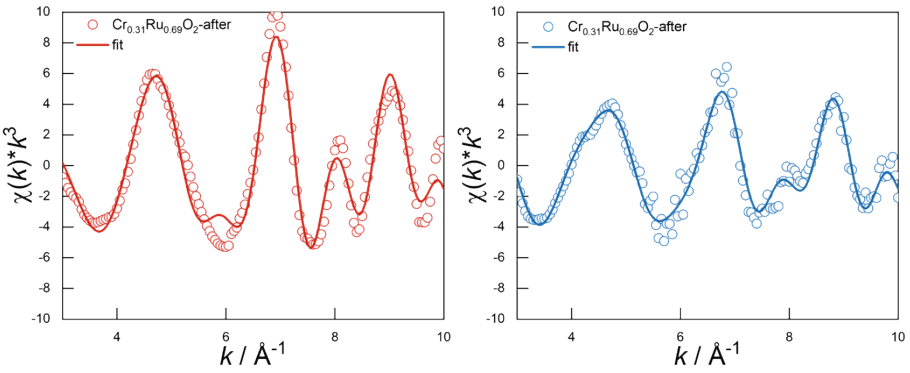

Fig. S18 k^3-weighted k space fitting curves of $Cr_{0.31}Ru_{0.69}O_2$-after and corresponding fitting curve.

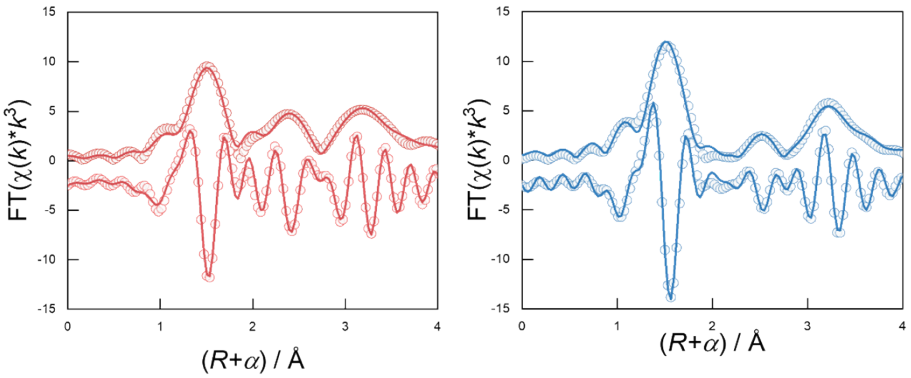

Fig. S19 k^3 -weighted Fourier transform and imaginary component spectra of $Cr_{0.31}Ru_{0.69}O_2$ and corresponding fitting curve. (a) Ru L_3-edge (FT range: 3.0-12.5 $Å^{-1}$; fitting range: 1.0-4.0 Å), (b) Cr L_3-edge (FT range: 3.0-13.0 $Å^{-1}$; fitting range: 1.0-4.0 Å).

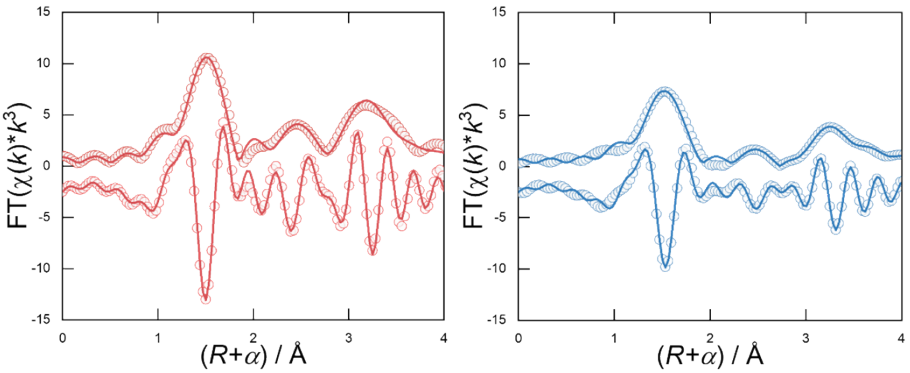

Fig. S20 k^3 -weighted Fourier transform and imaginary component spectra of $Cr_{0.31}Ru_{0.69}O_2$-after and corresponding fitting curve. (a) Ru L_3-edge (FT range: 3.0-12.5 $Å^{-1}$; fitting range: 1.0-3.7 Å), (b) Cr L_3-edge (FT range: 3.0-12.5 $Å^{-1}$; fitting range: 1.0-4.0 Å).

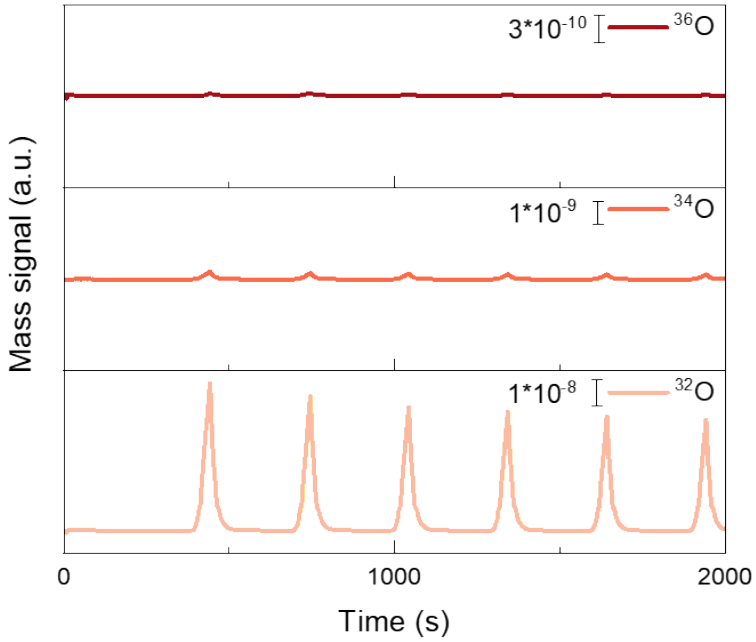

Fig. S21 DEMS signals of $^{32}O_2$, $^{34}O_2$ and $^{36}O_2$ collected during the CV cycle.

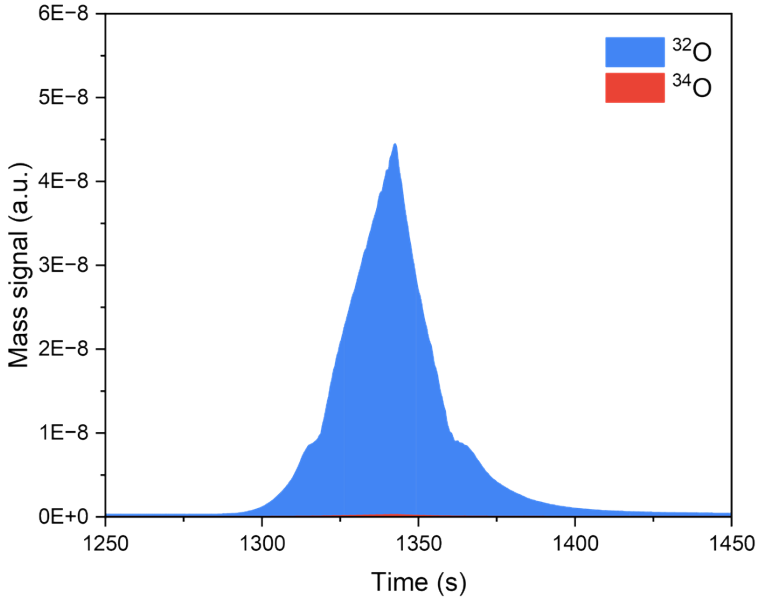

Fig. S22 The mass spectroscopy signals are baseline subtracted. $^{18}O=0.5*^{34}O/(^{34}O+^{32}O)*100\%= 0.26\%$.

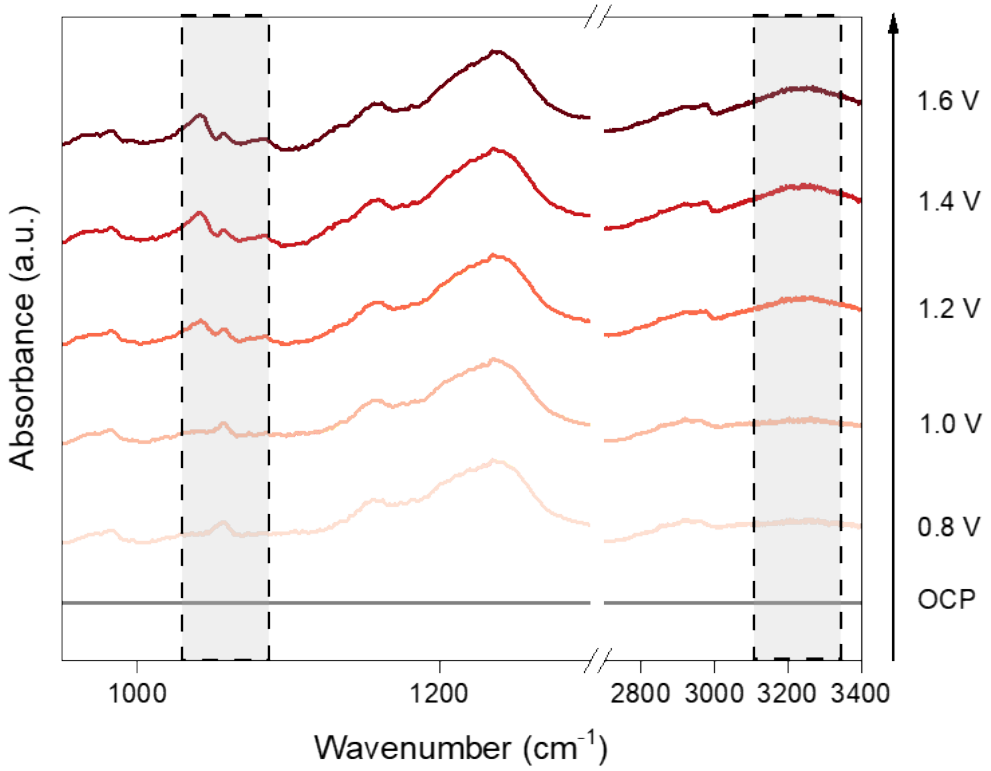

Fig. S23 In situ SEIRAS measurements under various potentials for $Cr_{0.31}Ru_{0.69}O_2$ electrocatalyst during the OER process.

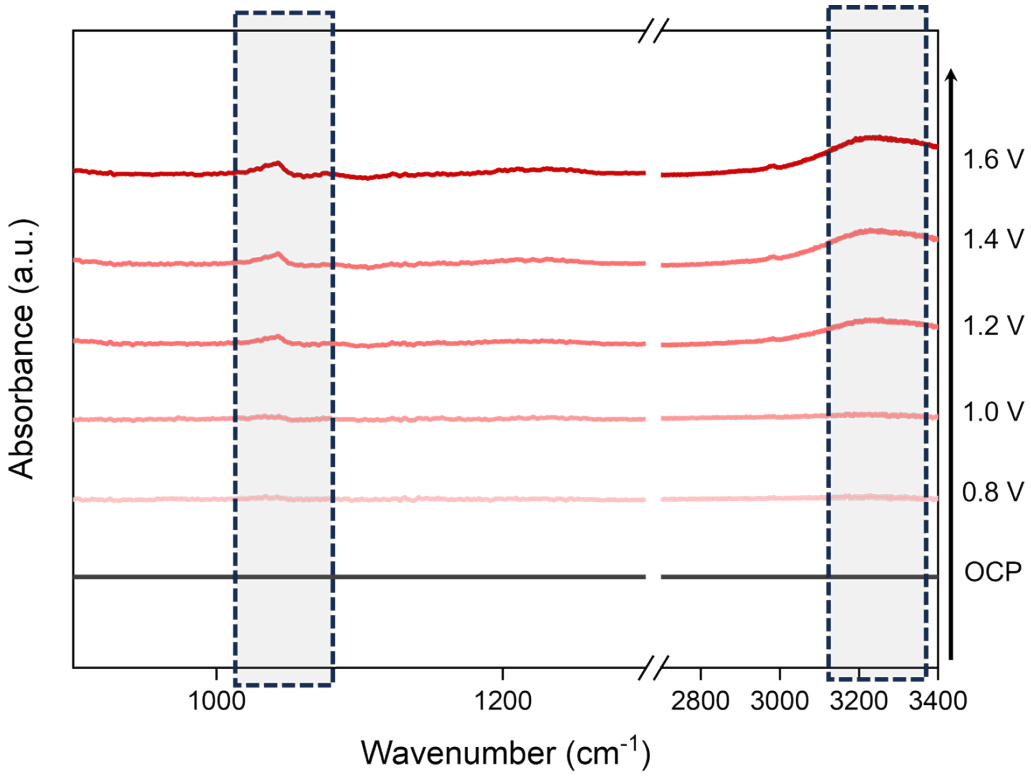

Fig. S24 In situ SEIRAS measurements under various potentials for commercial RuO_2 electrocatalyst during the OER process.

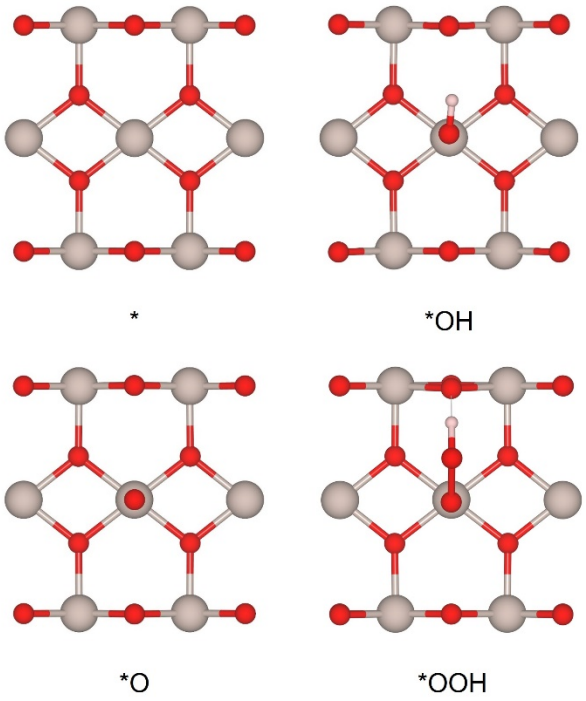

Fig. S25 Atomistic structures of RuO_2(011) surface with the adsorption of OER intermediates.

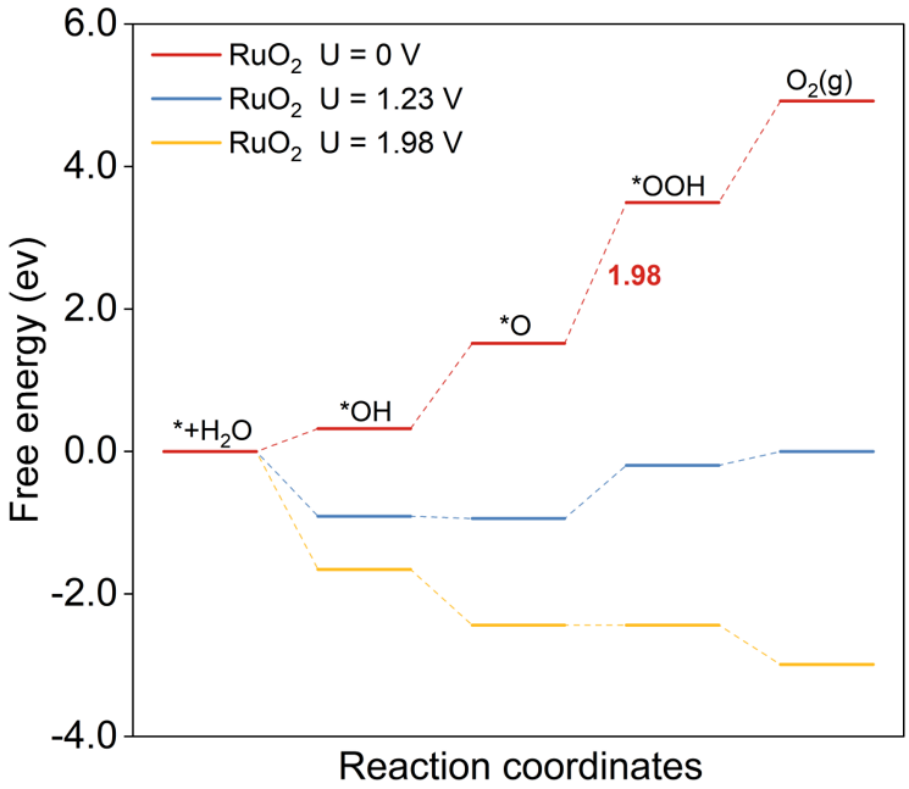

Fig. S26 Calculated OER free-energy diagrams on Ru site of RuO_2 at applied potentials of 0 V, 1.23 V, and 1.98 V verse reversible hydrogen electrode (RHE).

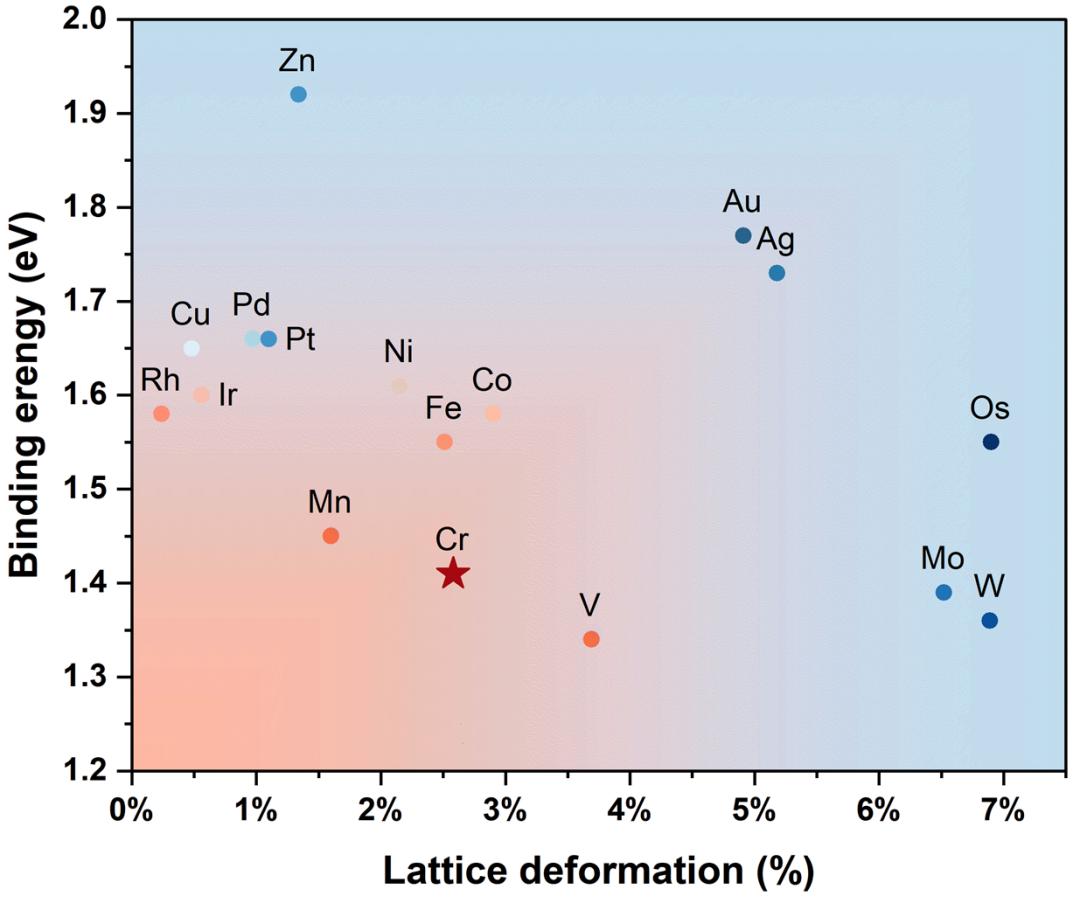

Fig. S27 Relationship between lattice deformation percentage and binding energy of RuO_2 doped with different metal atoms.

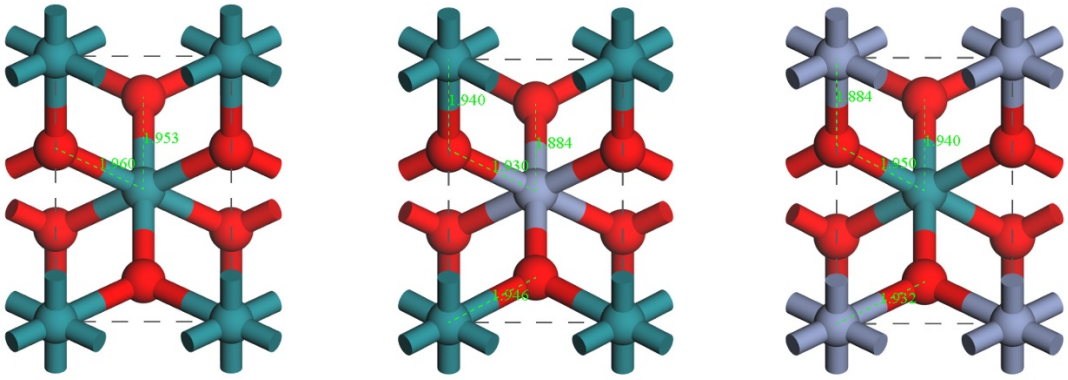

Fig. S28 Unit cell structures of RuO_2 and Cr-doped RuO_2 are used for calculations.

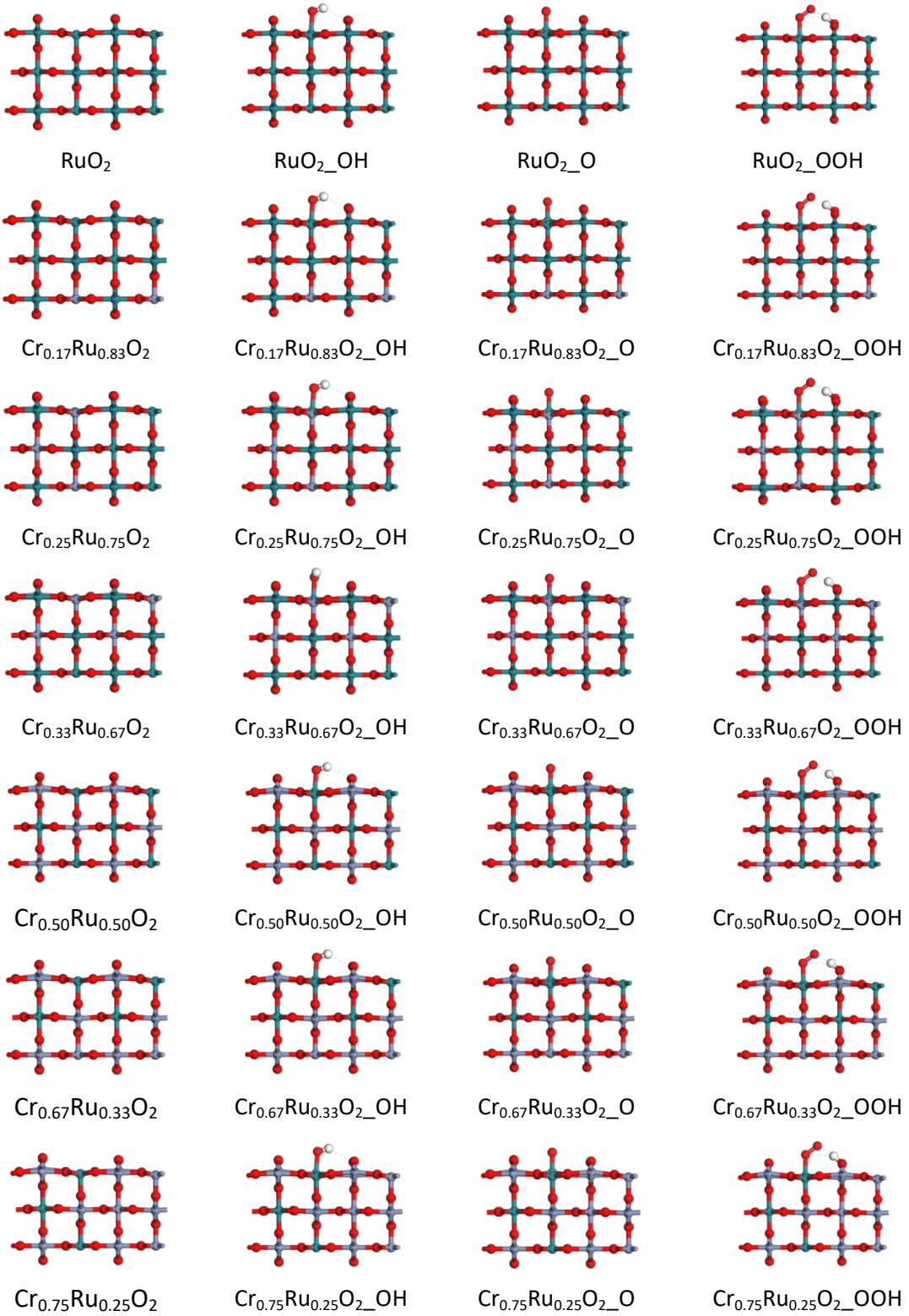

Fig. S29 DFT optimized structures of RuO_2, $Cr_{0.17}Ru_{0.83}O_2$, $Cr_{0.25}Ru_{0.75}O_2$, $Cr_{0.33}Ru_{0.67}O_2$, $Cr_{0.50}Ru_{0.50}O_2$, $Cr_{0.67}Ru_{0.33}O_2$ and $Cr_{0.75}Ru_{0.25}O_2$ corresponding *O, *OH and *OOH adsorption.

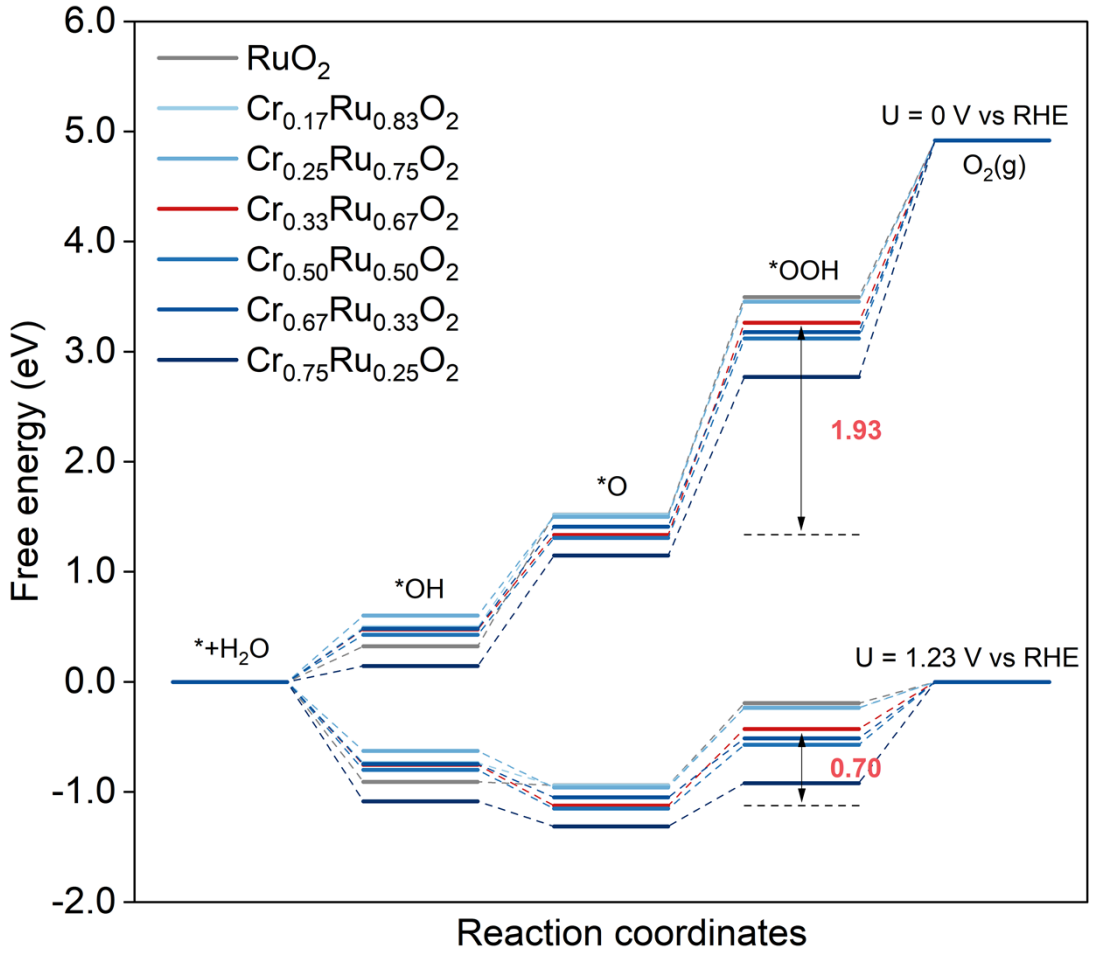

Fig. S30 Calculated OER free-energy diagrams for RuO_2, $Cr_{0.17}Ru_{0.83}O_2$, $Cr_{0.25}Ru_{0.75}O_2$, $Cr_{0.33}Ru_{0.67}O_2$, $Cr_{0.50}Ru_{0.50}O_2$, $Cr_{0.67}Ru_{0.33}O_2$ and $Cr_{0.75}Ru_{0.25}O_2$ at applied potentials of 0 V and 1.23 V vs. RHE.

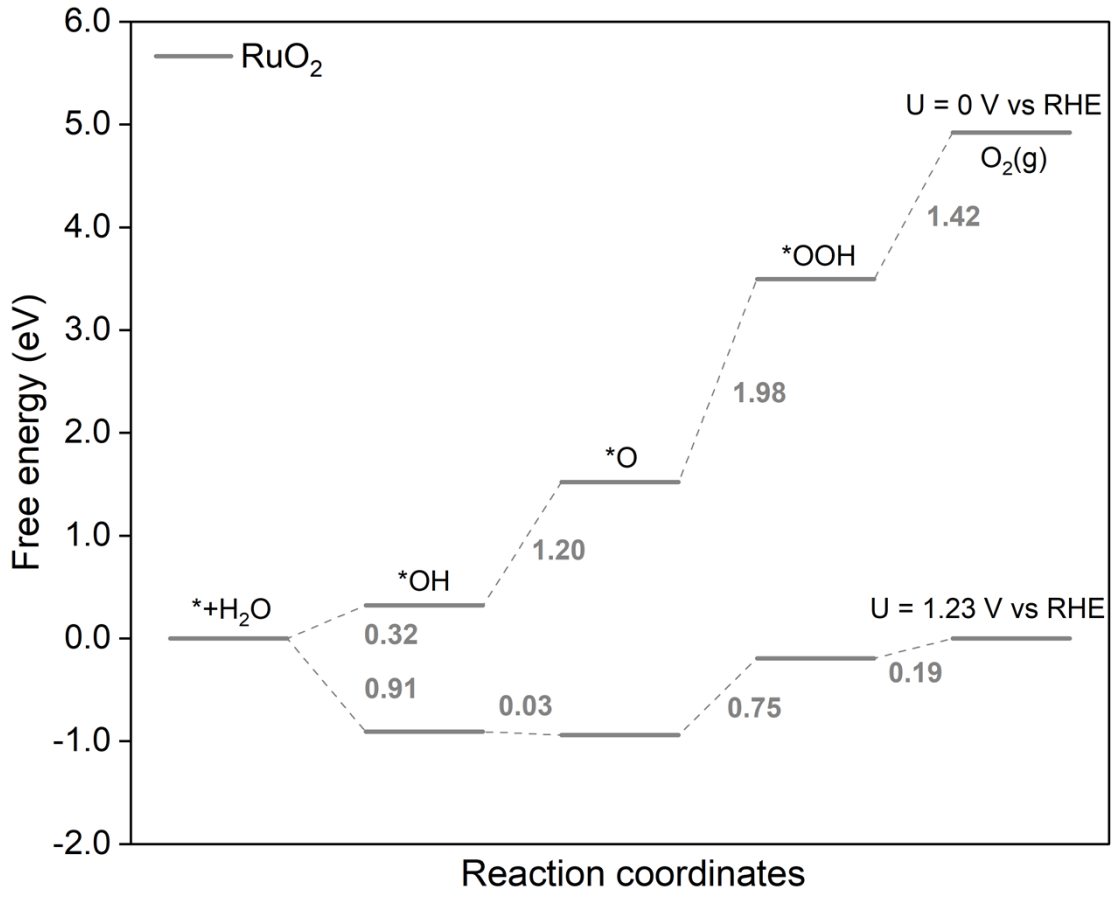

Fig. S31 The calculated free energy diagrams for RuO_2 at applied potentials of 0 V and 1.23 V vs. RHE.

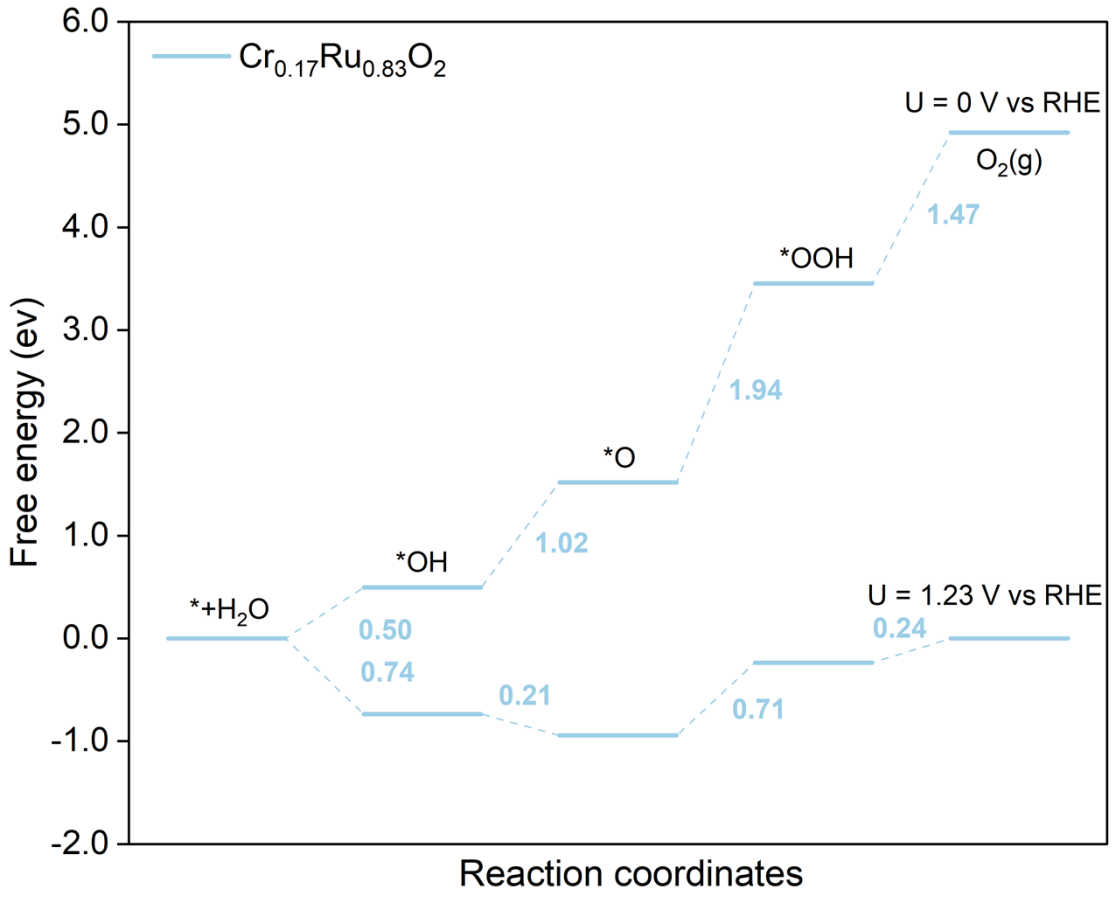

Fig. S32 The calculated free energy diagrams for $Cr_{0.17}Ru_{0.83}O_2$ at applied potentials of 0 V and 1.23 V vs. RHE.

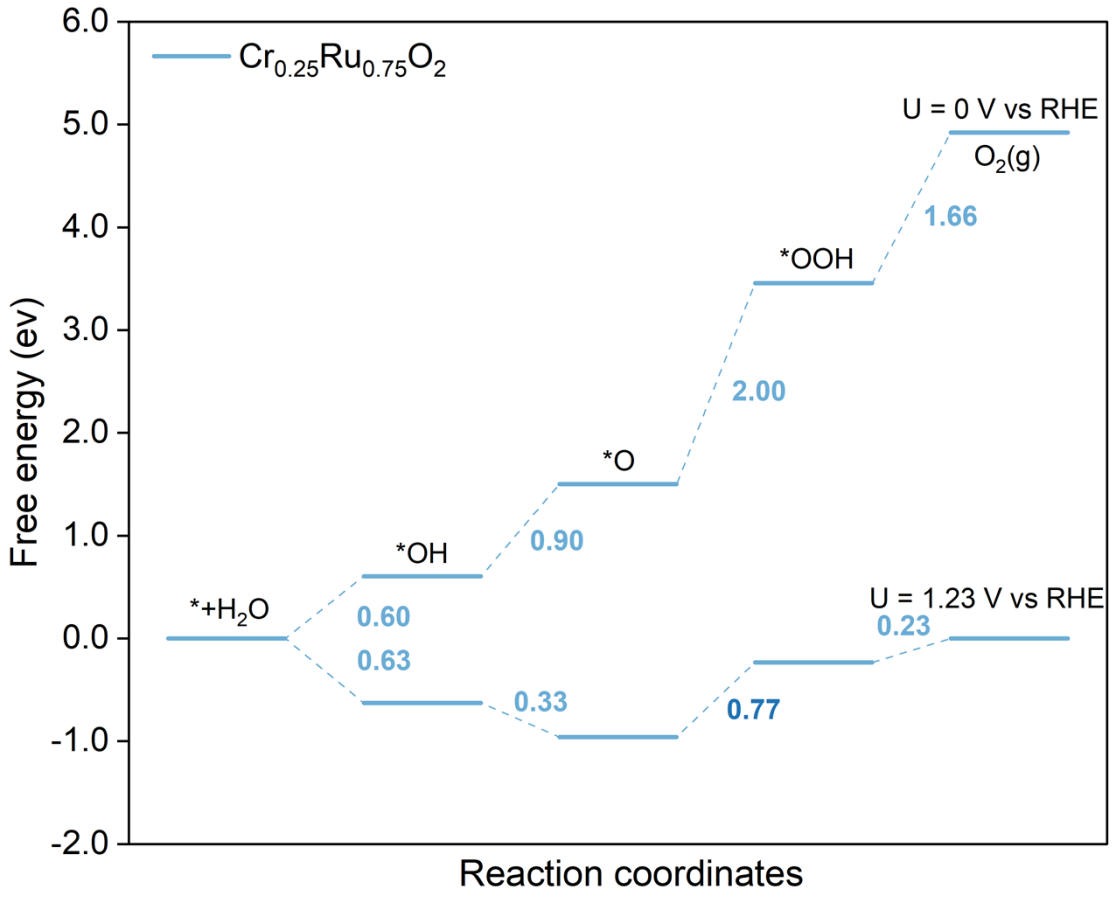

Fig. S33 The calculated free energy diagrams for $Cr_{0.25}Ru_{0.75}O_2$ at applied potentials of 0 V and 1.23 V vs. RHE.

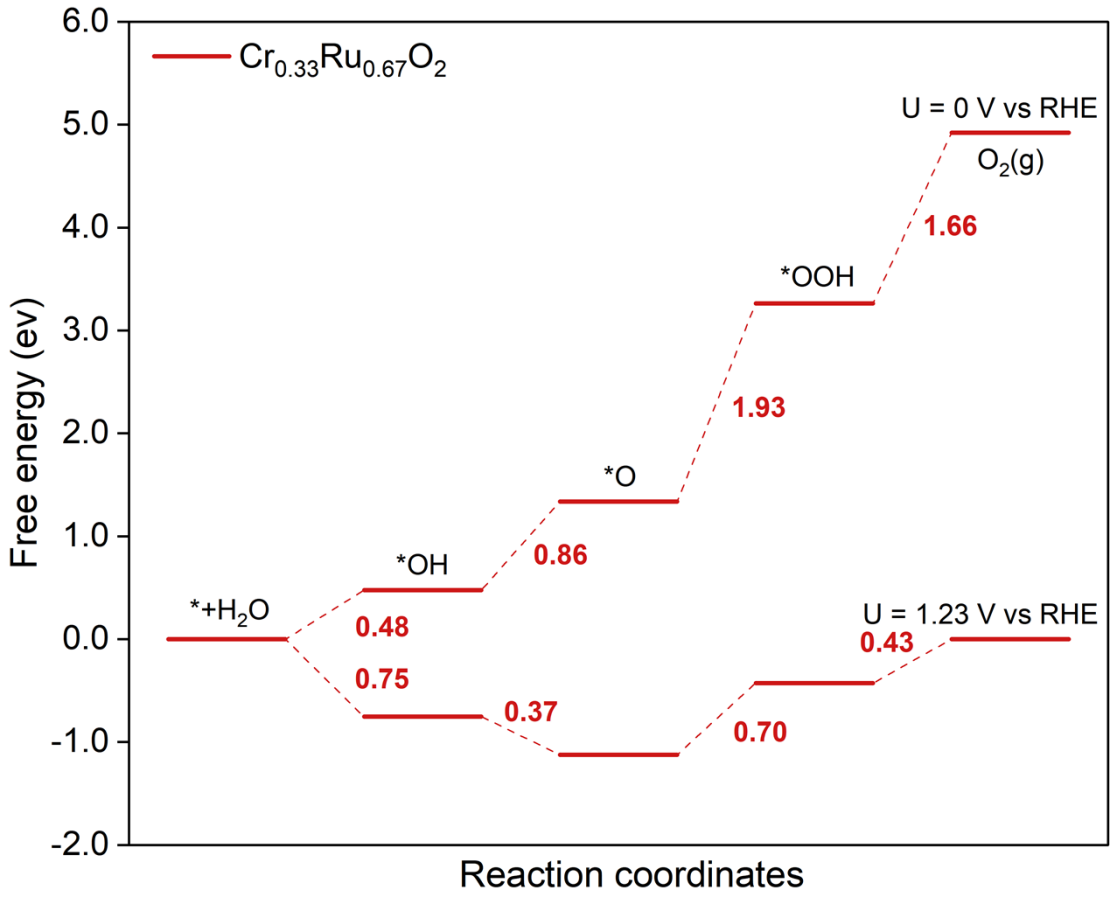

Fig. S34 The calculated free energy diagrams for $Cr_{0.33}Ru_{0.67}O_2$ at applied potentials of 0 V and 1.23 V vs. RHE.

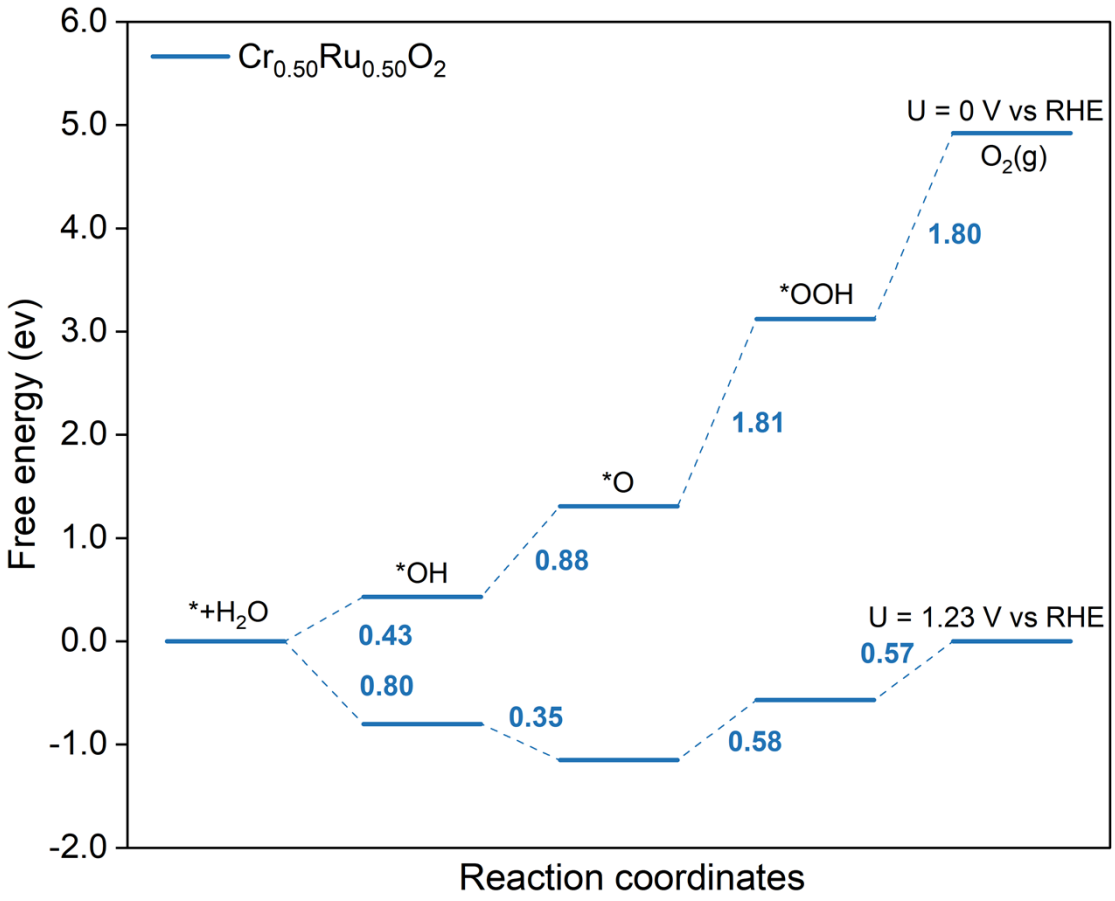

Fig. S35 The calculated free energy diagrams for $Cr_{0.50}Ru_{0.50}O_2$ at applied potentials of 0 V and 1.23 V vs. RHE.

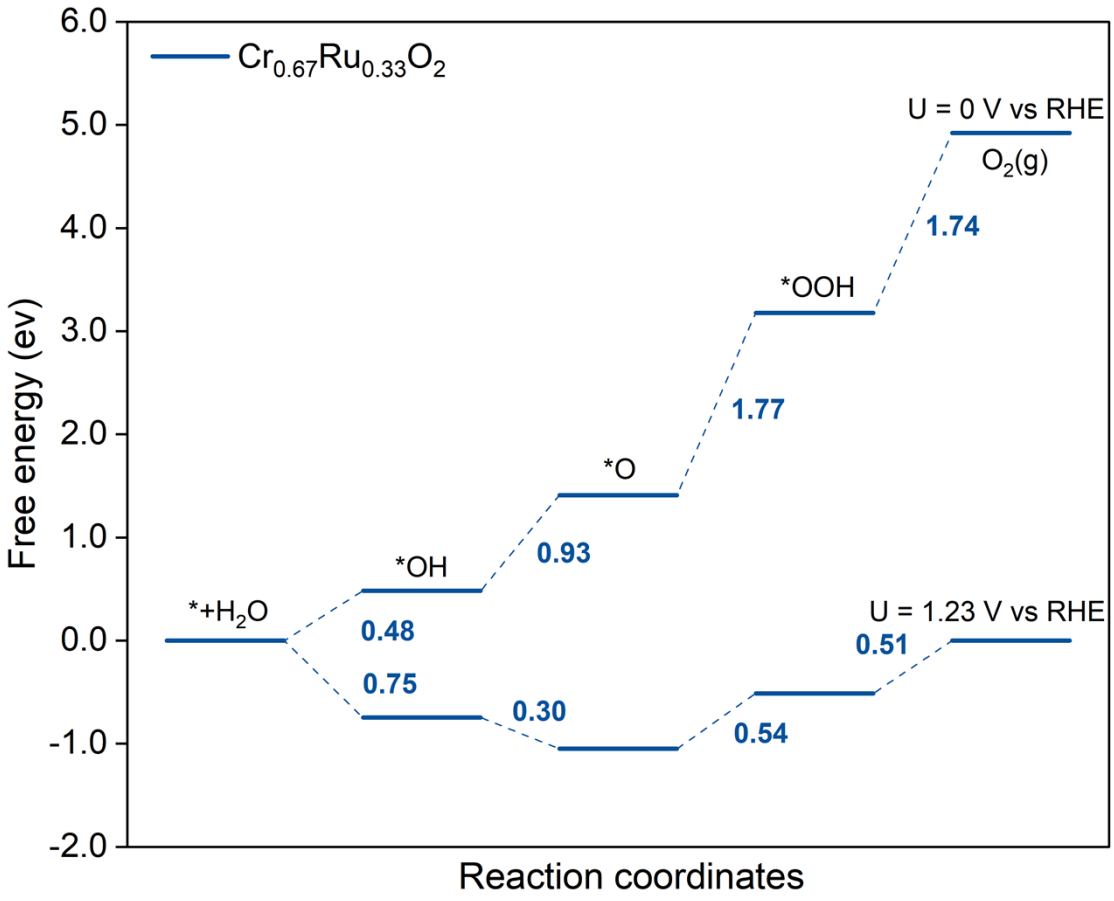

Fig. S36 The calculated free energy diagrams for $Cr_{0.67}Ru_{0.33}O_2$ at applied potentials of 0 V and 1.23 V vs. RHE.

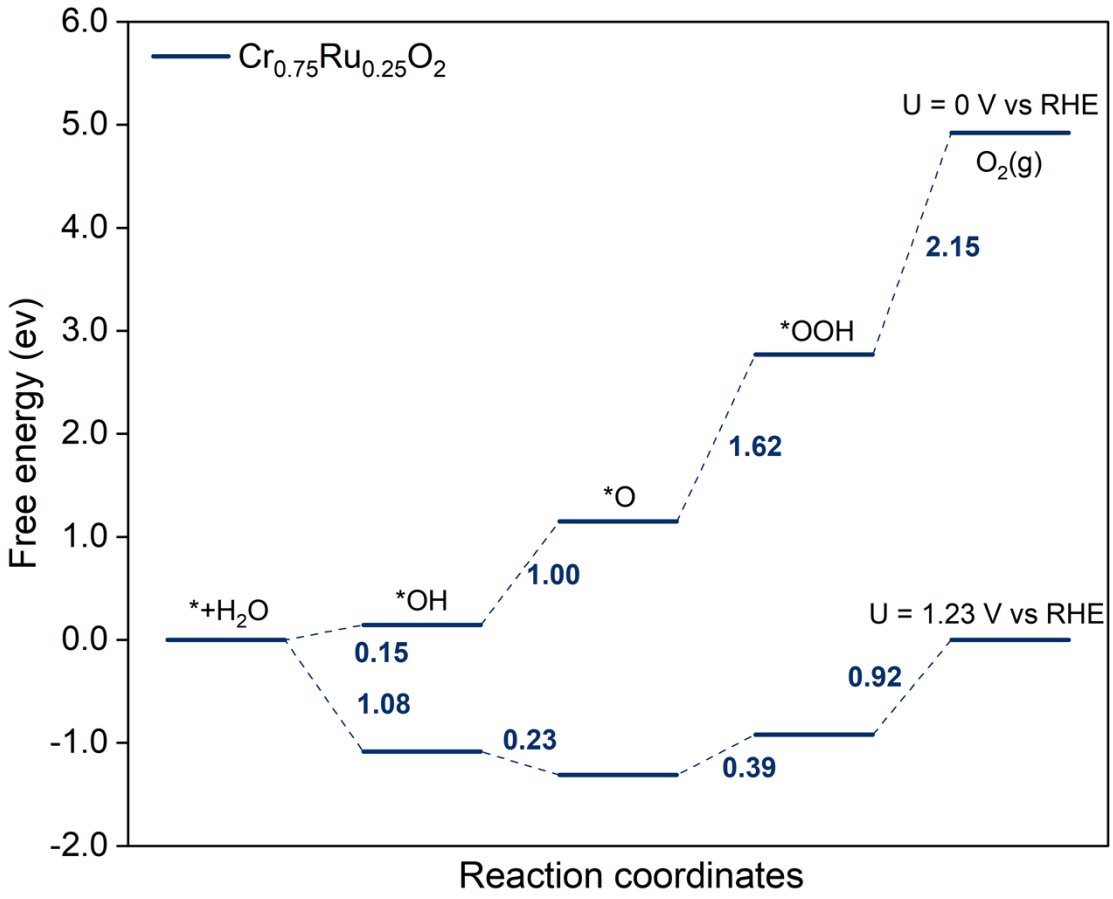

Fig. S37 The calculated free energy diagrams for $Cr_{0.75}Ru_{0.25}O_2$ at applied potentials of 0 V and 1.23 V vs. RHE.

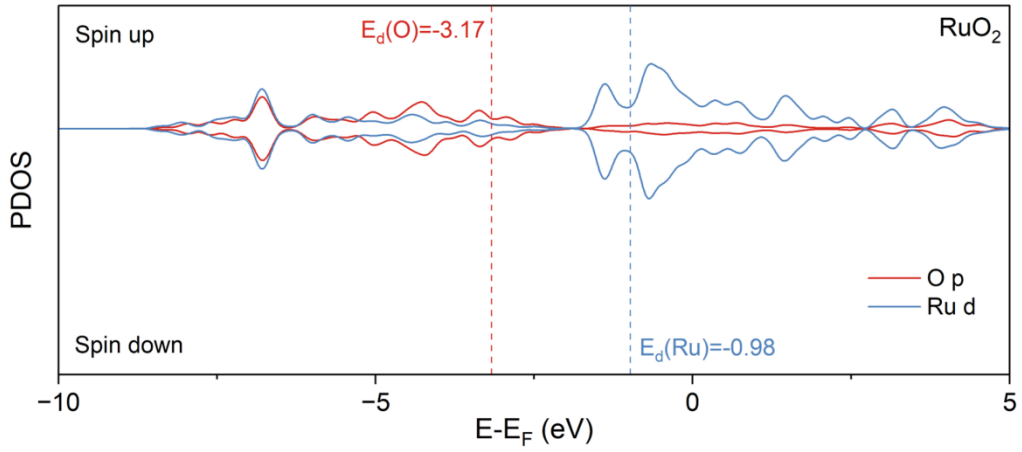

Fig. S38 PDOS of Ru 4d and O 2p-bands for RuO_2; corresponding d-band centers are denoted by dashed lines.

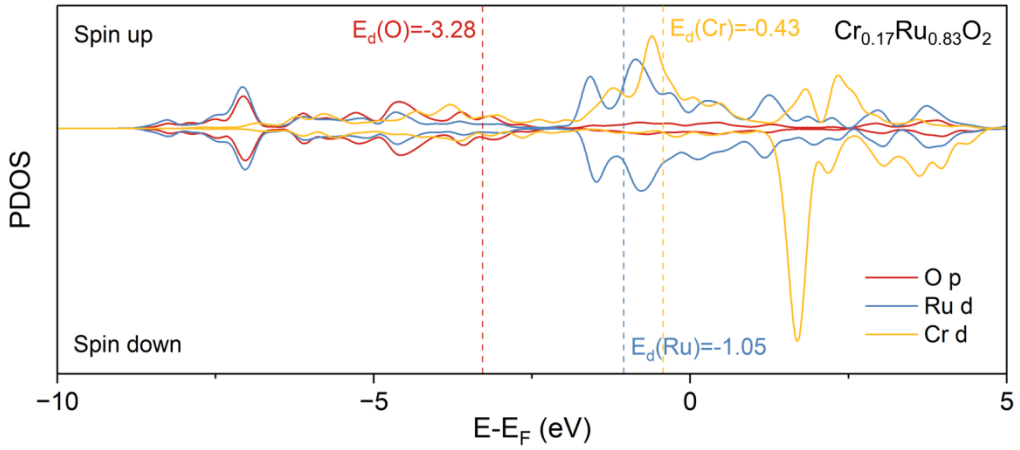

Fig. S39 PDOS of Ru 4d, O 2p and Cr 3d-bands for $Cr_{0.17}Ru_{0.83}O_2$; corresponding d-band centers are denoted by dashed lines.

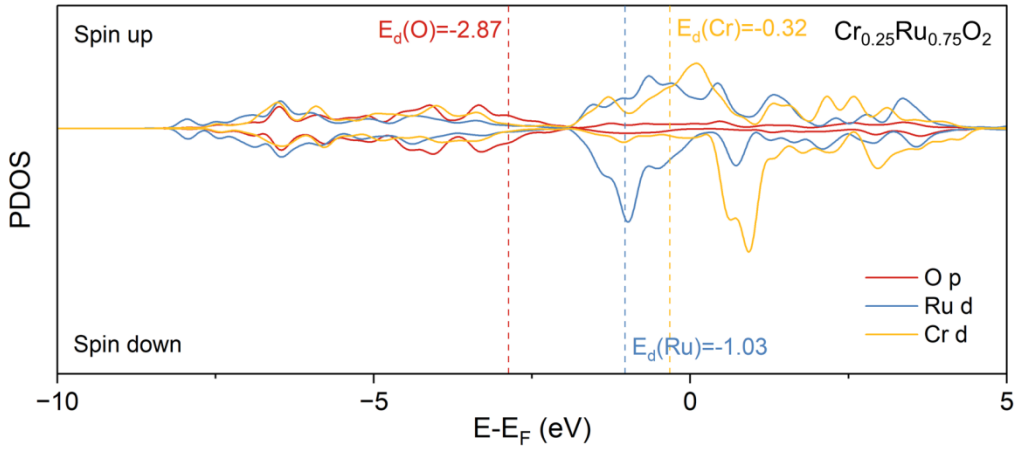

Fig. S40 PDOS of Ru 4d, O 2p and Cr 3d-bands for $Cr_{0.25}Ru_{0.75}O_2$; corresponding d-band centers are denoted by dashed lines.

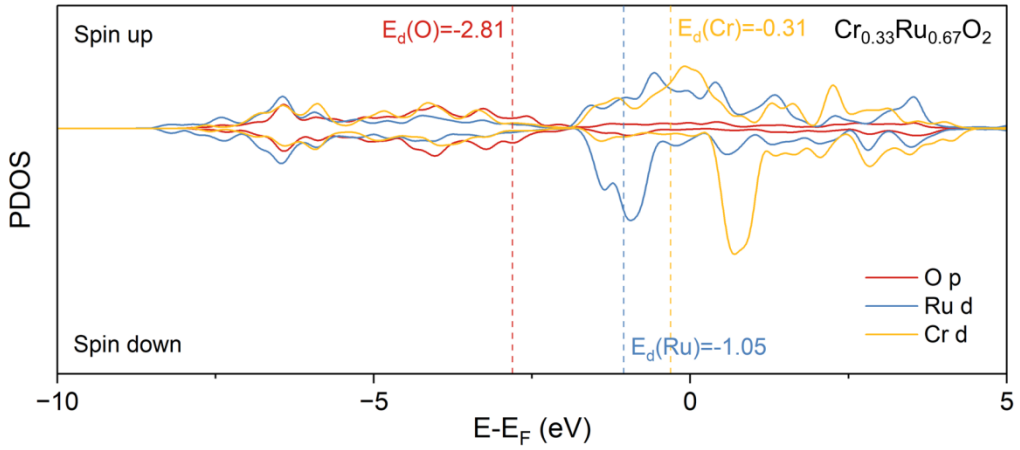

Fig. S41 PDOS of Ru 4d, O 2p and Cr 3d-bands for $Cr_{0.33}Ru_{0.67}O_2$; corresponding d-band centers are denoted by dashed lines.

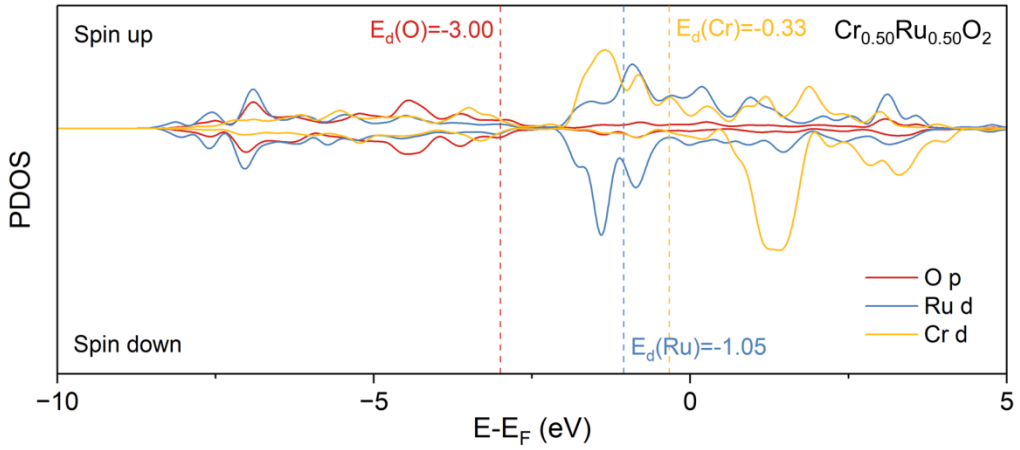

Fig. S42 PDOS of Ru 4d, O 2p and Cr 3d-bands for $Cr_{0.50}Ru_{0.50}O_2$; corresponding d-band centers are denoted by dashed lines.

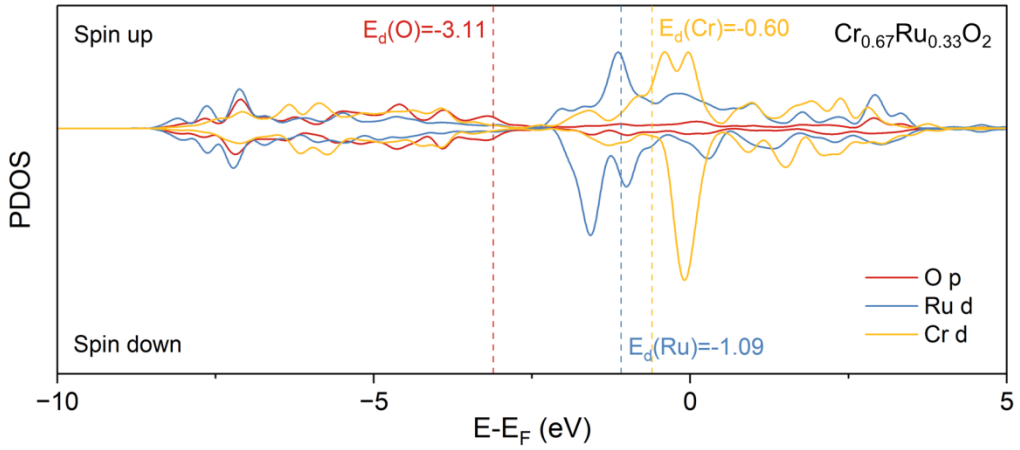

Fig. S43 PDOS of Ru 4d, O 2p and Cr 3d-bands for $Cr_{0.67}Ru_{0.33}O_2$; corresponding d-band centers are denoted by dashed lines.

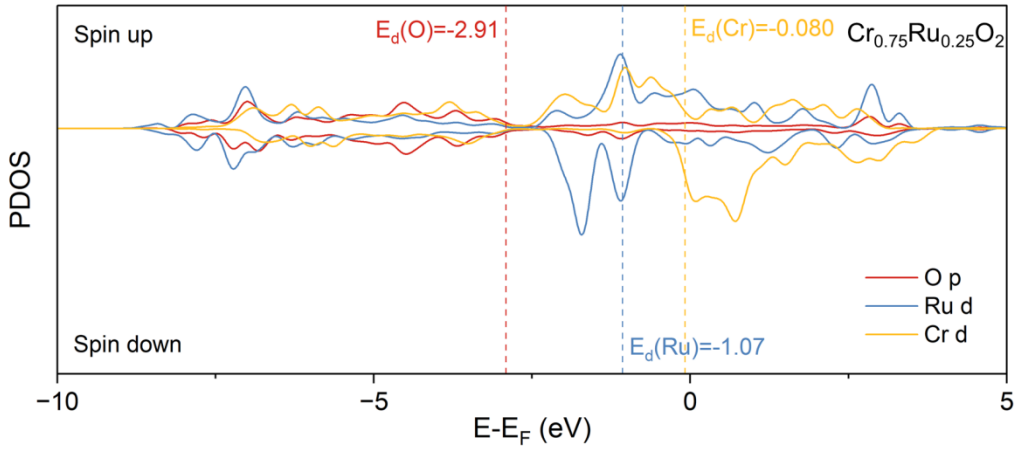

Fig. S44 PDOS of Ru 4d, O 2p and Cr 3d-bands for $Cr_{0.75}Ru_{0.25}O_2$; corresponding d-band centers are denoted by dashed lines.

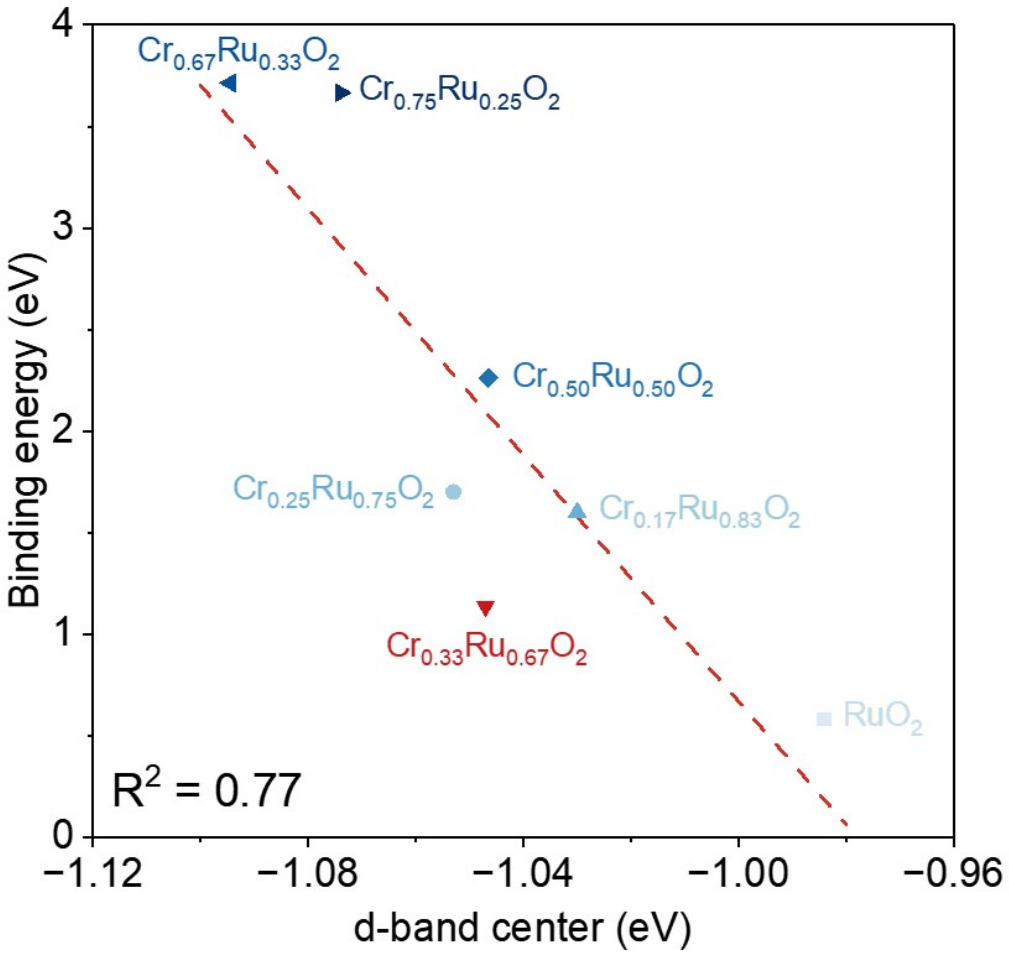

Fig. S45 The linear relationship between the d-band center of RuO_2, $Cr_{0.17}Ru_{0.83}O_2$, $Cr_{0.25}Ru_{0.75}O_2$, $Cr_{0.33}Ru_{0.67}O_2$, $Cr_{0.50}Ru_{0.50}O_2$, $Cr_{0.67}Ru_{0.33}O_2$ and $Cr_{0.75}Ru_{0.25}O_2$ and the binding energy of the Ru-O.

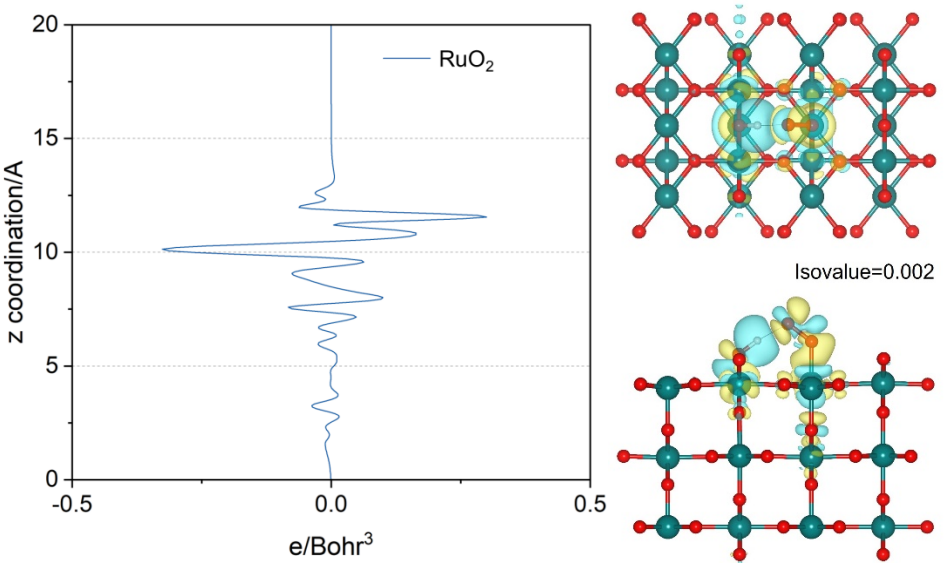

Fig. S46 The charge density differences of *OOH on RuO_2 (yellow: electron accumulation; cyan: electron depletion). The isosurfaces level is set as 0.002 e/bohr^3.

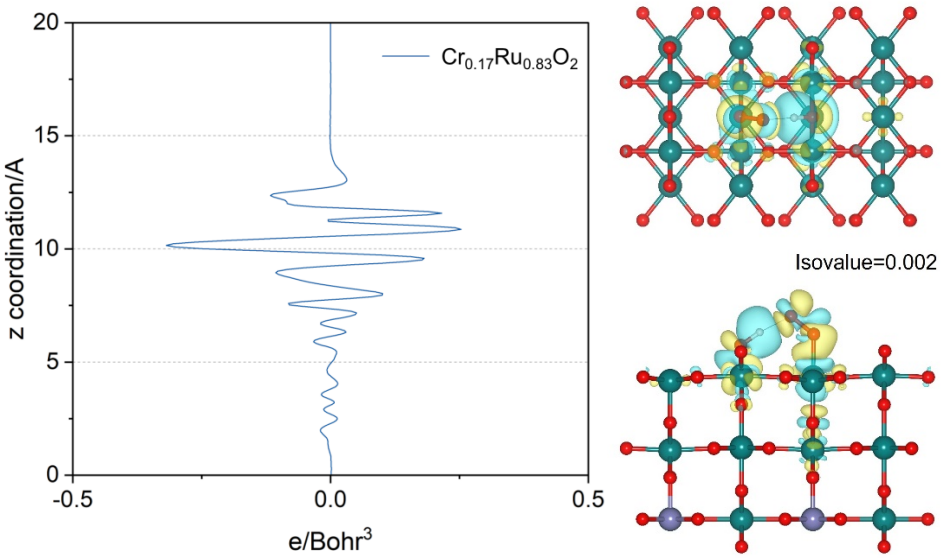

Fig. S47 The charge density differences of *OOH on $Cr_{0.17}Ru_{0.83}O_2$ (yellow: electron accumulation; cyan: electron depletion). The isosurfaces level is set as 0.002 e/bohr^3.

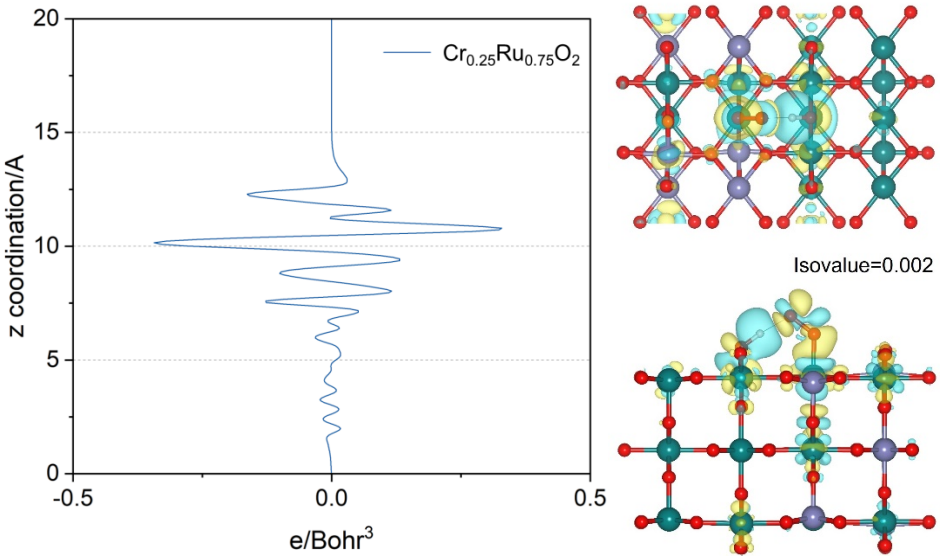

Fig. S48 The charge density differences of *OOH on $Cr_{0.25}Ru_{0.75}O_2$ (yellow: electron accumulation; cyan: electron depletion). The isosurfaces level is set as 0.002 e/bohr^3.

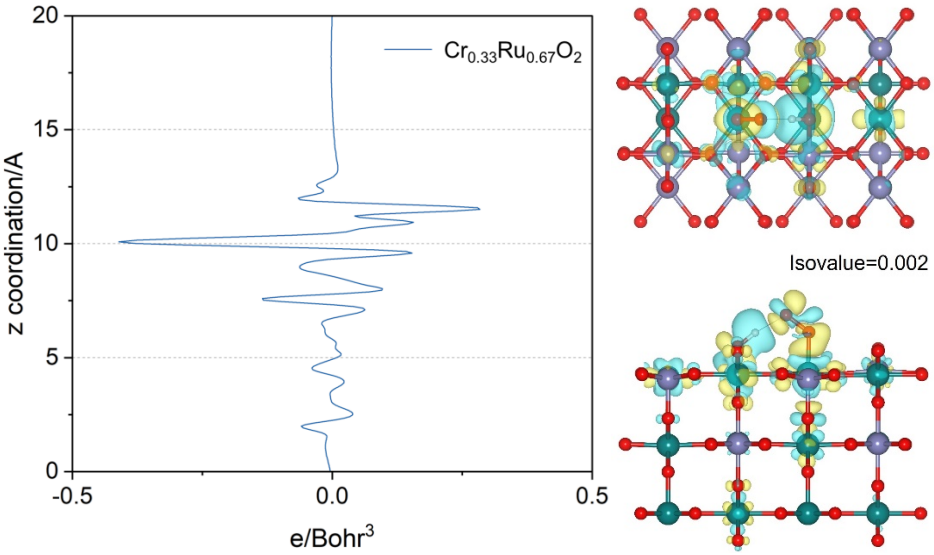

Fig. S49 The charge density differences of *OOH on $Cr_{0.33}Ru_{0.67}O_2$ (yellow: electron accumulation; cyan: electron depletion). The isosurfaces level is set as 0.002 e/bohr^3.

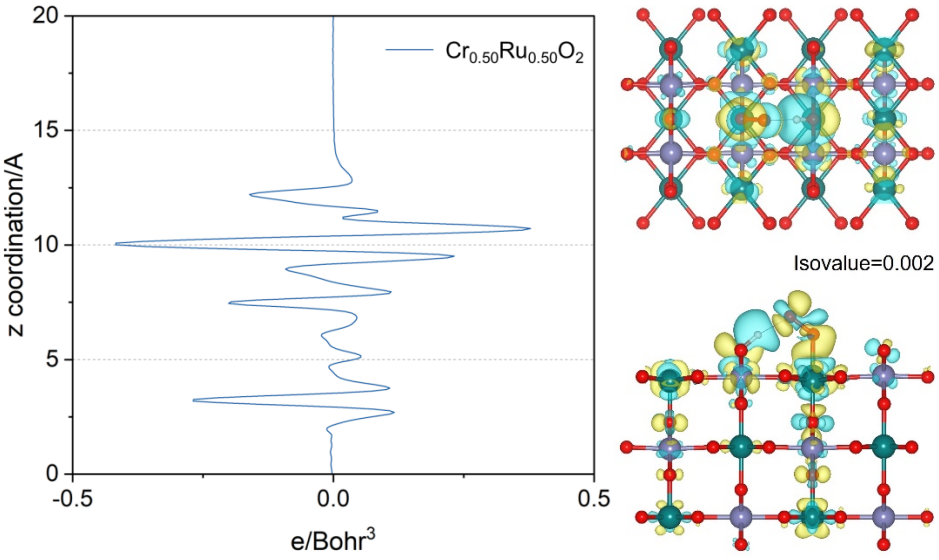

Fig. S50 The charge density differences of *OOH on $Cr_{0.50}Ru_{0.50}O_2$ (yellow: electron accumulation; cyan: electron depletion). The isosurfaces level is set as 0.002 e/bohr^3.

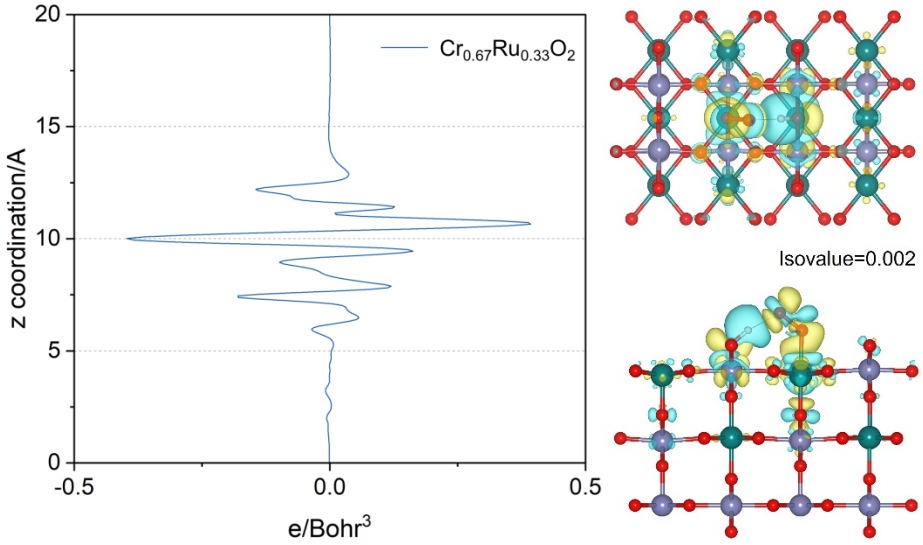

Fig. S51 The charge density differences of *OOH on $Cr_{0.67}Ru_{0.343}O_2$ (yellow: electron accumulation; cyan: electron depletion). The isosurfaces level is set as 0.002 e/bohr^3.

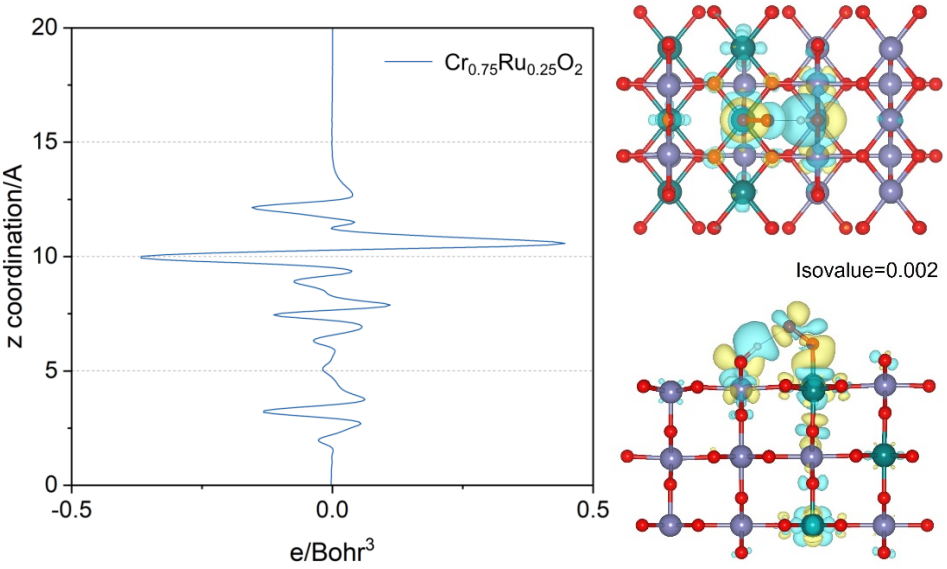

Fig. S52 The charge density differences of *OOH on $Cr_{0.75}Ru_{0.25}O_2$ (yellow: electron accumulation; cyan: electron depletion). The isosurfaces level is set as 0.002 e/bohr^3.

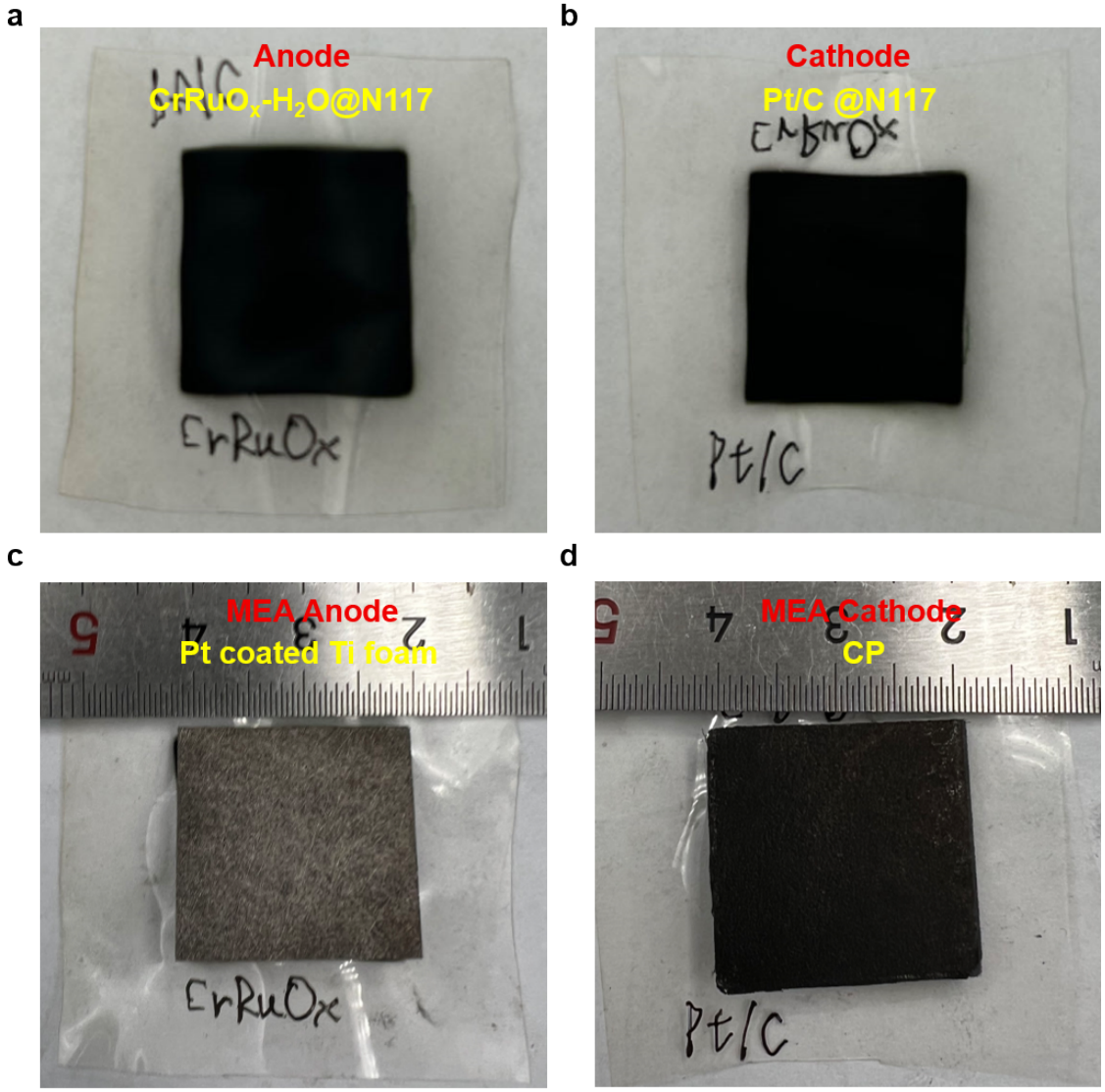

Fig. S53 Top view of (a) Anode catalyst layer, (b) Cathode catalyst layer, (C) gas diffusion layer of Anode, (d) gas diffusion layer of Cathode.

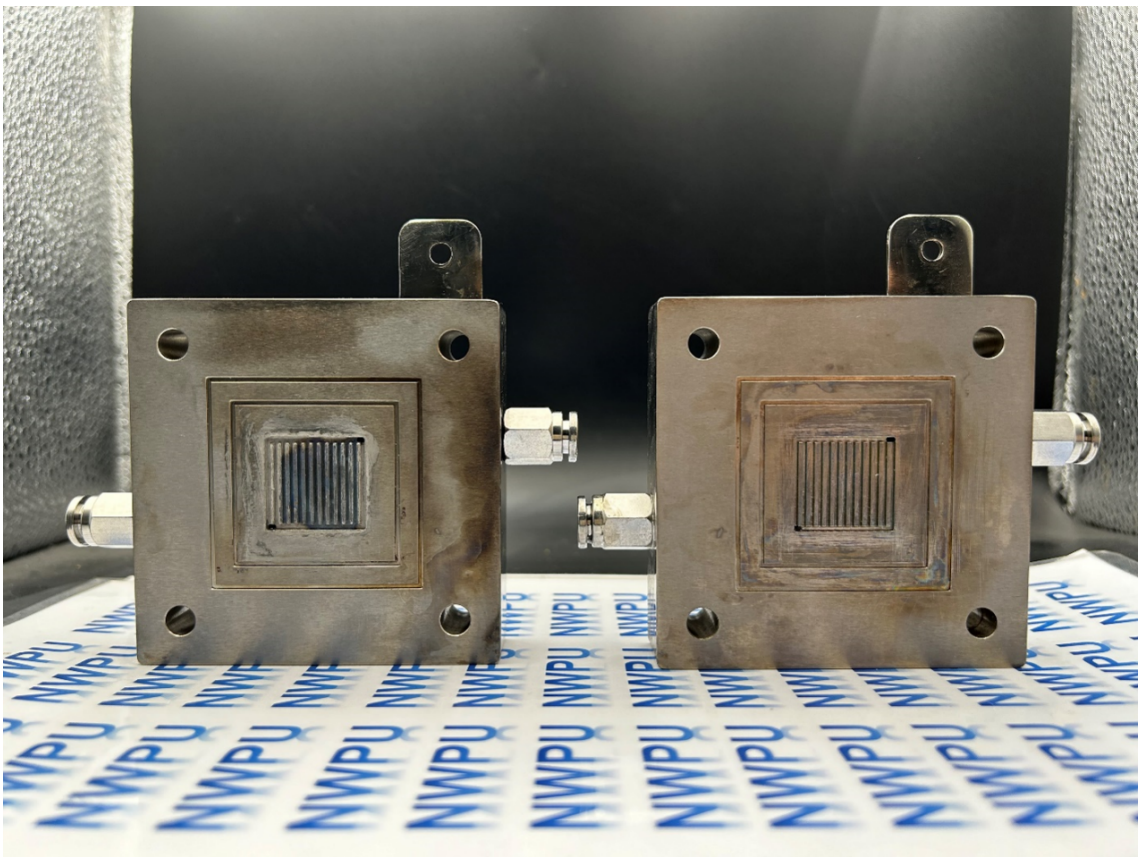

Fig. S54 Front view of bipolar plates (BP) with a flow field.

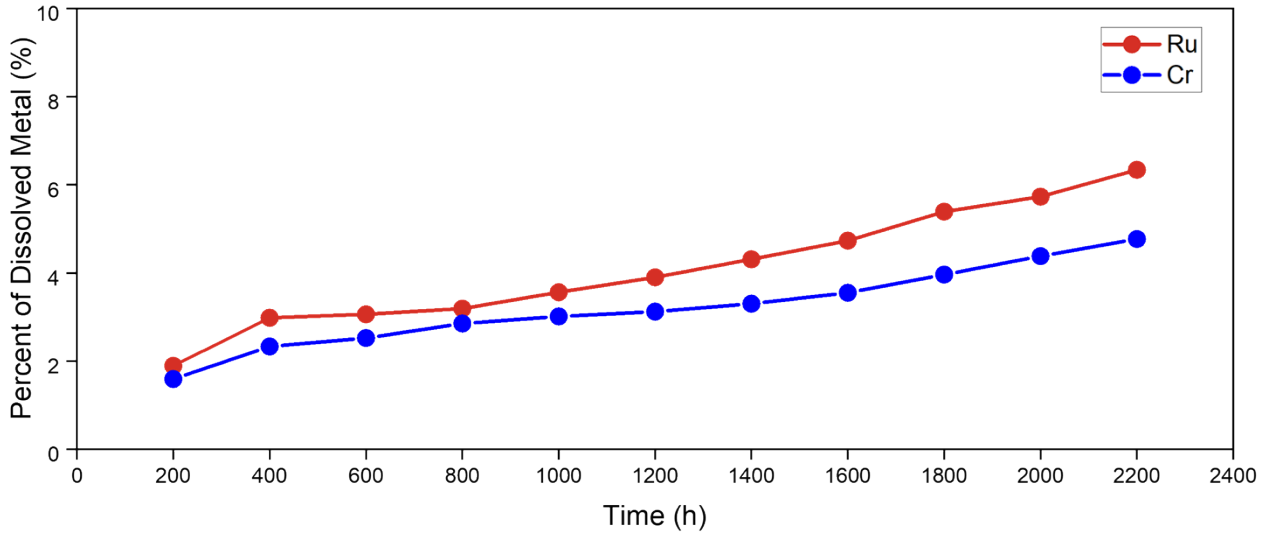

Fig. S55 Time-dependent ion dissolution of $Cr_{0.31}Ru_{0.69}O_2$ during PEMWE test.

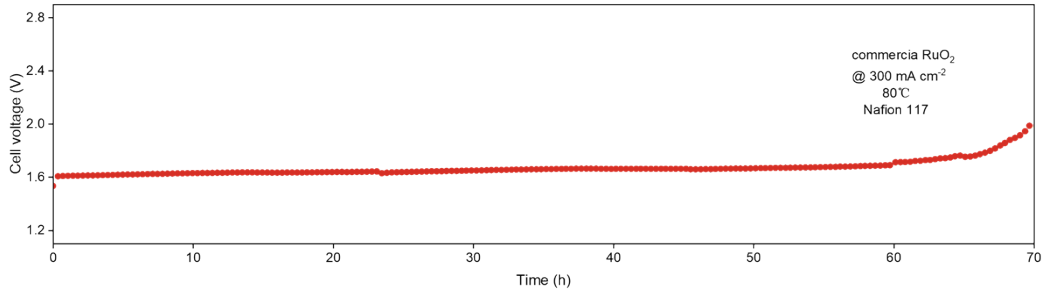

Fig. S56 Chronopotentiometry curve of the PEMWE using commercial RuO_2 catalysts operated at 300 mA cm^{-2}.

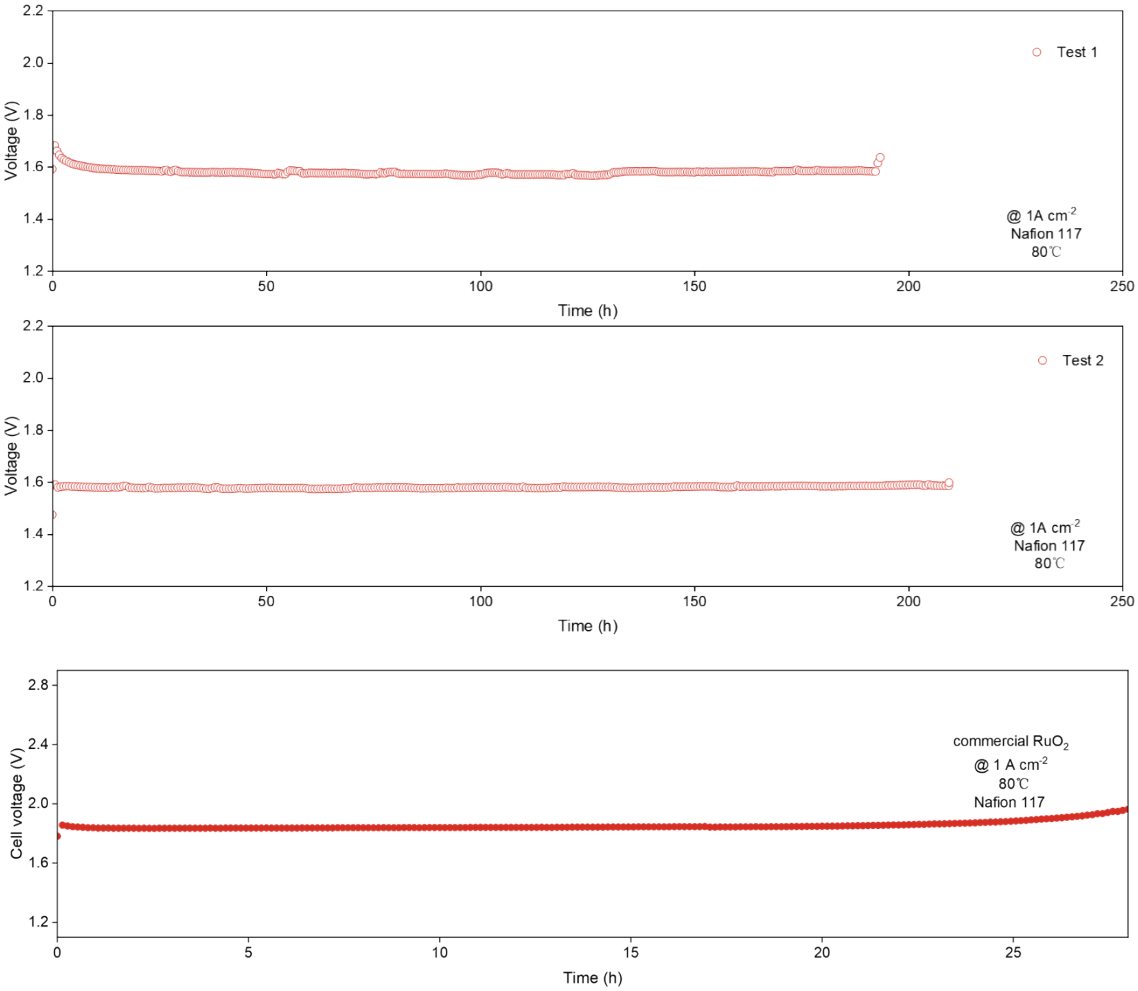

Fig. S57 Chronopotentiometry curve of the PEMWE using $Cr_{0.31}Ru_{0.69}O_2$ and commercial RuO_2 catalysts operated at 1 A cm^{-2}.

2.2 Supplementary Tables

Table S1. The mass fraction of Cr and Ru species for $Cr_xRu_{1-x}O_2$ catalysts measured by ICP-MS.

Catalysts	The Cr content (wt%)	The Ru content (wt%)	Ratio of Cr/Ru atoms (≈)
$\mathbf{Cr_{0.16}Ru_{0.84}O_2}$	6.65	67.9	16/84
$\mathbf{Cr_{0.22}Ru_{0.78}O_2}$	9.36	64.46	22/78
$\mathbf{Cr_{0.31}Ru_{0.69}O_2}$	13.68	59.15	31/69
$\mathbf{Cr_{0.48}Ru_{0.52}O_2}$	22.8	47.97	48/52
$\mathbf{Cr_{0.64}Ru_{0.36}O_2}$	32.74	35.77	64/36
$Cr_{0.71}Ru_{0.29}O_2$	37.59	29.82	71/29

Table S2. Lattice parameters of $Cr_{0.31}Ru_{0.69}O_2$.

Formula	$Cr_{0.31}Ru_{0.69}O_2$
Crystal system	tetragonal
Space group	P 42/m n m
a/Å	4.49307
b/Å	4.49307
c/Å	3.10639
α	90
β	90
γ	90
Cell volume/ Å^3	62.7

Table S3. Structural Parameters for $Cr_{0.31}Ru_{0.69}O_2$, $Cr_{0.31}Ru_{0.69}O_2$-after, Ru foil, Cr foil, RuO_2 bulk and CrO_2 bulk extracted from the EXAFS fitting. (S_0^2=0.9)

Sample	Shell	N	*R* (Å)	σ^2 (10^{-3} Å^2)	ΔE_0 (eV)	*R*-factor
$Cr_{0.31}Ru_{0.69}O_2$	Ru-O	3.48	1.97±0.01	2.1±1.9	3.66	0.025
	Ru-Ru	2.03	2.73±0.02	6.9±4.4		
	Ru-O-Ru	0.01	3.62±0.08	20.2±9.3		
	Ru-O-Cr	1.99	3.57±0.10	2.7±6.7		
$Cr_{0.31}Ru_{0.69}O_2$-after	Ru-O	3.35	1.97±0.01	2.9±2.2	1.73	0.024
	Ru-Ru	1.61	2.73±0.02	7.0±7.4		
	Ru-O-Ru	0.06	3.47±0.06	19.6±6.5		
	Ru-O-Cr	3.94	3.51±0.10	0.6±2.6		
$Cr_{0.31}Ru_{0.69}O_2$	Cr-O	3.56	1.94±0.06	1.7±1.4	4.30	0.03
	Cr-Cr	0.04	2.94±0.03	5.4±9.8		
	Cr-O-Cr	0.16	3.38±0.06	10.3±8.7		
$Cr_{0.31}Ru_{0.69}O_2$-after	Cr-O	3.17	1.94±0.07	3.6±1.3	3.89	0.021
	Cr-Cr	0.09	2.99±0.08	11.1±8.9		
	Cr-O-Cr	0.44	3.32±0.10	4.3±4.7		
Ru-foil	$Ru-Ru_1$	6*	2.67±0.01	2.8±0.9	2.86	0.006
	$Ru-Ru_2$	6*	3.82±0.01	7.8±6.3		
RuO_2	Ru-O	4*	1.96±0.02	0.9±0.7	2.09	0.019
	Ru-Ru	2*	3.16±0.05	0.3±1.4		
	Ru-O-Ru	8*	3.42±0.1	14.3±6.2		
	Ru-O-Ru	4*	3.71±0.05	9.2±1.4		
Cr-foil	$Cr-Cr_1$	8	2.49±0.01	6.4±1.9	4.26	0.002
	$Cr-Cr_2$	6	2.86±0.02	4.9±2.1		
CrO_2	Cr-O	4*	1.90±0.01	2.6±0.8	4.98	0.023
	Cr-Cr	2*	2.95±0.04	4.5±1.7		
	Cr-O-Cr	8*	3.49±0.05	5.6±1.2		

S_0^2 is the amplitude reduction factor;

N is the coordination number;

R is interatomic distance (the bond length between central atoms and surrounding coordination atoms);

σ^2 is Debye-Waller factor (a measure of thermal and static disorder in absorber-scatterer distances);

ΔE_0 is edge-energy shift (the difference between the zero kinetic energy value of the sample and that of the theoretical model).

R factor is used to value the goodness of the fitting.[8] *This value was fixed during EXAFS fitting, based on the known structure of Ru and Cr foil, RuO_2 and CrO_2 bulk.

Table S4. ECSA parameters for different catalysts.

Catalyst	C_{dl} (F)	ECSA (cm^2_{ECSA})	Roughness factor (R_f)
RuO_2	0.00813	232.2857	1185.1312
$Cr_{0.16}Ru_{0.84}O_2$	0.01123	320.8571	1637.0262
$Cr_{0.22}Ru_{0.78}O_2$	0.01354	386.8571	1,973.7609
$Cr_{0.31}Ru_{0.69}O_2$	0.02484	709.7142	3620.9912
$Cr_{0.48}Ru_{0.52}O_2$	0.01446	413.1429	2,107.8717
$Cr_{0.64}Ru_{0.36}O_2$	0.01068	305.1429	1,556.8513
$Cr_{0.71}Ru_{0.29}O_2$	0.00941	268.8571	1371.7201
Com RuO_2	0.00558	159.4286	813.4111

Table S5. The comparison of OER stability of $Cr_{0.31}Ru_{0.69}O_2$ with recently reported electrocatalysts in acid media.

Catalysts	Stability (h)@10 mA/cm^{-2}	Δη (mV)	Decay rate (mV h^{-1})	References
$Cr_{0.31}Ru_{0.69}O_2$	**＞1400**	**20**	**0.014**	**This work**
Com-RuO_2	28	390	13.929	This work
py-RuO_2: Zn	1000	153	0.153	9
Cu-RuO_2	8	83	10.375	10
$Cr_{0.6}Ru_{0.4}O_2$	10	70	7.000	11
Ru_1-Pt_3Cu	28	30	1.071	12
$CaCu_3Ru_4O_{12}$	24	21	0.875	13
$Nd_{0.1}$RuOx/CC	25	15	0.600	14
Mn-RuO_2	10	150	15.000	15
NC@Vo·-RuO_2/CNTs-350	900	15	0.017	16
E-Ru/Fe ONAs	9	50	5.556	17
$W_{0.2}Er_{0.1}Ru_{0.7}O_{2-\delta}$	500	83	0.166	18
$Ru_{(anc)}$-Co_3O_4	150	38	0.253	19
Ni-RuO_2	205	20	0.097	20
ac-$Cr_{0.53}Ru_{0.47}O_{2-\delta}$	40	/	/	21
RuO_2/BNNS	350	25	0.071	22
GB-RuO_2	140	42	0.300	23
$RuNi_2$@G-250	24	21	0.875	24

Table S6. Unit cell volume, bond length and formation energy of RuO_2 and Cr-doped RuO_2.

	RuO_2	Cr_RuO_2	Cr_RuO_{2_2}
Volume (Å^3)	58.58	57.51	57.73
Bond length (Ru-O) (Å)	1.95/1.96	1.94/1.95	1.94/1.95
Bond length (Cr-O) (Å)	-	1.88/1.93	1.88/1.93
Formation energy (eV)	-4.45	-6.53	-6.53

Table S7. The correction of zero point energy of the adsorbed.

	*OH (eV)	*O (eV)	*OOH (eV)
RuO_2	0.30	0.06	0.37
$Cr_{0.17}Ru_{0.83}O_2$	0.31	0.06	0.41
$Cr_{0.25}Ru_{0.75}O_2$	0.31	0.06	0.36
$Cr_{0.33}Ru_{0.67}O_2$	0.35	0.06	0.38
$Cr_{0.50}Ru_{0.50}O_2$	0.30	0.04	0.38
$Cr_{0.67}Ru_{0.33}O_2$	0.30	0.05	0.39
$Cr_{0.75}Ru_{0.25}O_2$	0.31	0.05	0.41

Table S8. The comparison of PEMWE stability and activity of $Cr_{0.31}Ru_{0.69}O_2$ with recently reported electrocatalysts.

	Cell voltage@1A cm^{-2}(V)	Durability (h)	References
$Cr_{0.31}Ru_{0.69}O_2$	1.56	2300	**This work**
Nb-RuO_2	1.69	100	25
Ni-RuO_2	1.95	1000	20
(Ru–W)O_x	1.62	500	26
$SnRuO_x$	1.565	1300	27
$Ba_{0.3}(SO_4)_\delta W_{0.2}Ru_{0.5}O_{2-\delta}$	1.68	300	28
GB-RuO_2	1.54	100	23

Notes and references

1. G. Kresse and J. Hafner, *Phys. Rev. B Condens. Matter*, 1994, **49**, 14251-14269.
2. G. Kresse and J. Furthmüller, *Comput. Mater. Sci.*, 1996, **6**, 15-50.
3. G. Kresse and D. P. Joubert, *Phys. Rev. B*, 1999, **59**, 1758-1775.
4. P. E. Blöchl, O. Jepsen and O. K. Andersen, *Phys. Rev. B*, 1994, **49**, 16223-16233.
5. J. Klimeš, D. R. Bowler and A. Michaelides, *Phys. Rev. B*, 2011, **83**, 195131.
6. J. K. Nørskov, T. Bligaard, A. Logadottir, J. R. Kitchin, J. G. Chen, S. Pandelov and U. Stimming, *J. Electrochem. Soc.*, 2005, **152**, J23.
7. G. Henkelman, A. Arnaldsson and H. Jónsson, *Comput. Mater. Sci.*, 2006, **36**, 354-360.
8. B. Ravel and M. Newville, *J. Synchrot. Radiat.*, 2005, **12**, 537-541.
9. D. Zhang, M. Li, X. Yong, H. Song, G. I. N. Waterhouse, Y. Yi, B. Xue, D. Zhang, B. Liu and S. Lu, *Nat. Commun.*, 2023, **14**, 2517.
10. J. Su, R. Ge, K. Jiang, Y. Dong, F. Hao, Z. Tian, G. Chen and L. Chen, *Adv. Mater.*, 2018, **30**, 1801351.
11. Y. Lin, Z. Tian, L. Zhang, J. Ma, Z. Jiang, B. J. Deibert, R. Ge and L. Chen, *Nat. Commun.*, 2019, **10**, 162.
12. Y. Yao, S. Hu, W. Chen, Z.-Q. Huang, W. Wei, T. Yao, R. Liu, K. Zang, X. Wang, G. Wu, W. Yuan, T. Yuan, B. Zhu, W. Liu, Z. Li, D. He, Z. Xue, Y. Wang, X. Zheng, J. Dong, C.-R. Chang, Y. Chen, X. Hong, J. Luo, S. Wei, W.-X. Li, P. Strasser, Y. Wu and Y. Li, *Nat. Catal.*, 2019, **2**, 304-313.
13. X. Miao, L. Zhang, L. Wu, Z. Hu, L. Shi and S. Zhou, *Nat. Commun.*, 2019, **10**, 3809.
14. L. Li, G. Zhang, J. Xu, H. He, B. Wang, Z. Yang and S. Yang, *Adv. Funct. Mater.*, 2023, **33**.
15. S. Chen, H. Huang, P. Jiang, K. Yang, J. Diao, S. Gong, S. Liu, M. Huang, H. Wang and Q. Chen, *ACS Catal.*, 2020, **10**, 1152-1160.
16. H. Yan, Z. Jiang, B. Deng, Y. Wang and Z.-J. Jiang, *Adv. Energy Mater.*, 2023, **13**, 2300152.
17. Q. Yao, B. Huang, Y. Xu, L. Li, Q. Shao and X. Huang, *Nano Energy*, 2021, **84**, 105909.
18. S. Hao, M. Liu, J. Pan, X. Liu, X. Tan, N. Xu, Y. He, L. Lei and X. Zhang, *Nat. Commun.*, 2020, **11**, 5368.
19. Y. Hao, S.-F. Hung, W.-J. Zeng, Y. Wang, C. Zhang, C.-H. Kuo, L. Wang, S. Zhao, Y. Zhang, H.-Y. Chen and S. Peng, *J. Am. Chem. Soc.*, 2023, **145**, 23659-23669.
20. Z.-Y. Wu, F.-Y. Chen, B. Li, S.-W. Yu, Y. Z. Finfrock, D. M. Meira, Q.-Q. Yan, P. Zhu, M.-X. Chen, T.-W. Song, Z. Yin, H.-W. Liang, S. Zhang, G. Wang and H. Wang, *Nat. Mater.*, 2023, **22**, 100-108.
21. X. Zhao, Z. Li, H. Jang, X. Wei, L. Wang, M. G. Kim, J. Cho, X. Liu and Q. Qin, *Small*, 2024, **n/a**, 2311172.
22. Y. Hao, S.-F. Hung, C. Tian, L. Wang, Y.-Y. Chen, S. Zhao, K.-S. Peng, C. Zhang, Y. Zhang, C.-H. Kuo, H.-Y. Chen and S. Peng, *Angew. Chem. Int. Ed.*, 2024**n/a**, e202402018.
23. W. He, X. Tan, Y. Guo, Y. Xiao, H. Cui and C. Wang, *Angew. Chem. Int. Ed.*, 2024, **63**, e202405798.
24. X. Cui, P. Ren, C. Ma, J. Zhao, R. Chen, S. Chen, N. P. Rajan, H. Li, L. Yu, Z. Tian and D. Deng, *Adv. Mater.*, 2020, **32**, 1908126.
25. H. Liu, Z. Zhang, J. Fang, M. Li, M. G. Sendeku, X. Wang, H. Wu, Y. Li, J. Ge, Z. Zhuang, D. Zhou, Y. Kuang and X. Sun, *Joule*, 2023, **7**, 558-573.
26. L. Deng, S.-F. Hung, Z.-Y. Lin, Y. Zhang, C. Zhang, Y. Hao, S. Liu, C.-H. Kuo, H.-Y. Chen, J. Peng, J. Wang and S. Peng, *Adv. Mater.*, 2023, **35**, 2305939.
27. Z. Shi, J. Li, Y. Wang, S. Liu, J. Zhu, J. Yang, X. Wang, J. Ni, Z. Jiang, L. Zhang, Y. Wang, C. Liu, W. Xing and J. Ge, *Nat. Commun.*, 2023, **14**, 843.
28. Y. Xue, J. Zhao, L. Huang, Y.-R. Lu, A. Malek, G. Gao, Z. Zhuang, D. Wang, C. T. Yavuz and X. Lu, *Nat. Commun.*, 2023, **14**, 8093.

